Nanoplastics Weathering and Polycyclic

2 Aromatic Hydrocarbon Mobilization

```
Erik B. Schiferle<sup>1,2,3</sup>, Wenxu Ge<sup>1,2</sup>, and Björn M. Reinhard<sup>1,2,3*</sup>
 3
 4
       <sup>1</sup>Department of Chemistry, <sup>2</sup>The Photonics Center, <sup>3</sup>Division of Materials Science and
 5
       Engineering, Boston University, Boston, MA, 02215, USA.
 6
 7
 8
       * Email bmr@bu.edu
 9
10
11
12
13
14
15
16
17
18
19
20
21
22
23
24
25
26
```

ABSTRACT

Despite increasing efforts to recycle plastic materials, large quantities of plastics waste continue to accumulate in the oceans. Persistent mechanical and photochemical degradation of plastics in the oceans yield micro- and nano-scale plastic particles, which represent potential vectors for mobilizing hydrophobic carcinogens in an aqueous milieu. Yet, the fate and potential threats associated with plastics remain largely unexplored. Herein, we apply an accelerated weathering protocol to consumer plastics to characterize the effect of photochemical weathering on the size, morphology, and chemical composition of nanoplastics under defined conditions and validate that the photochemical degradation is consistent with plastics harvested from the Pacific Ocean. Machine learning algorithms trained with accelerated weathering data successfully classify weathered plastics from nature. We demonstrate that photodegradation of polyethylene terephthalate (PET)containing plastics produces enough CO₂ to induce a mineralization process that results in the deposition of CaCO₃ on nanoplastics. Finally, we determine that despite UV-radiation induced photochemical degradation and mineral deposition, nanoplastics retain their ability to sorb, mobilize, and increase bioaccessibility of polycyclic aromatic hydrocarbons (PAHs) in water and under simulated physiological gastric and intestinal conditions.

KEYWORDS: nanoplastics, carcinogen, bioaccessibility, polycyclic aromatic hydrocarbons (PAHs), environment, plastic waste

Plastics are synthetic materials made up of polymers, which due to their low cost and highly tunable material properties have pervaded virtually all aspects of everyday life. As of 2020, 367 million tons of plastic are produced annually, while an estimated total of 3.8 billion tons of plastic products have been produced since 1950.² Alarmingly, only an estimated 9% of the total plastics by mass are recycled as of 2019.³⁻⁶ As many commodity plastics do not biodegrade to a significant degree, the inevitable consequence of the enormous scale of anthropogenic plastic use is a widespread accumulation of plastics in the marine environment.⁷⁻¹¹ When exposed to the elements, macroscopic plastic objects weather and become brittle, resulting in a fragmentation into smaller pieces. Independent of their exact chemical composition, synthetic polymer fragments with dimensions smaller than 5 mm are collectively referred to as microplastics, 2, 12 while even smaller plastic particles with dimensions between 1 - 1000 nm are referred to as nanoplastics. ¹³ Although the impact of micro- to nano-sized plastics on the biota are still insufficiently understood, reports of decreased sperm motility, birth defects, intestinal membrane damage, organ toxicity, bioaccumulation, and even death in fish, 14-16 zebrafish, 15, 17 crustacean, 18 mice, 15, ^{19,20} and humans²¹ give reasons for concern. Studies investigating human health are limited, but hundreds of micro-sized plastic particles were detected in stool samples.²² Especially in the case of nanoplastics, with their large surface to volume ratios, the potential for direct detrimental interactions between nanoplastics and living organisms is augmented by a potential role as a transport vector for hydrophobic contaminants, including carcinogens such as polycyclic aromatic hydrocarbons (PAHs).²³⁻²⁷

80

81

82

83

84

85

86

87

88

89

90

59

60

61

62

63

64

65

66

67

68

69

70

71

72

73

74

7576

77

78

79

PAHs are byproducts of an incomplete combustion of organic matter. The concentration of PAHs in marine ecosystems has increased due to anthropogenic activity. Importantly, they are carcinogens, known to increase the probability of skin, lung, bladder, liver, and stomach cancers. PAHs have very low aqueous solubility and are primarily associated with natural organic matter particles, such as sediment, in an aqueous environment. Recent studies have reported a nearly a 25-fold microplastics-associated increase of hydrophobic persistent organic pollutants (POPs) in seawater and orders of magnitude higher bioaccumulation of PAHs and other hydrophobic organic chemicals in tissue. The capacity of nanoscale plastic particles to mobilize PAHs is, however, less studied, even though an increasing surface-to-volume ratio with decreasing size may enhance PAH

sorption. The increasing quantities of micro- and nano-sized plastics in aquatic ecosystems raise important questions about interactions between PAHs and plastic particles, in particular, their potential relevance in mobilizing PAHs. The potential for increased nanoplastics-mediated bioaccessibility of PAHs is determined by the capacity of PAHs to sorb onto nanoplastics in the environment and to release, or desorb, from the nanoplastics in the gastrointestinal tract.³³ Increased bioaccessibility would have direct implications for the bioaccumulation of PAHs. Desorption of PAHs could also be aided by nanoplastics transport across intestinal membranes, which has been demonstrated with PET nanoplastics experimentally.³⁴ PAH sorption and desorption properties depend on the size, structure, chemical composition, as well as the surface properties of the plastic particles. While "large" millimeter to micrometer sized particles can show significant absorption, adsorption becomes dominant for smaller particle sizes. The large surface-to-volume ratio of nanoparticles is in principle conducive to the adsorption of hydrophobic PAHs, but the impact of environmental weathering processes on surface properties and bioaccessibility remain insufficiently understood.

In this work, we apply an accelerated weathering protocol to consumer plastics to characterize the effect of photochemical weathering on the chemical composition of nanoplastics and to validate that these changes are consistent with plastics harvested from nature. Our findings show that despite UV-radiation induced photochemical degradation and mineral deposition, nanoplastics retain the capacity to sorb PAHs after weathering and that nanoplastics can increase the concentration of PAHs in water by up to 3 orders of magnitude. In addition, we test how these photochemical changes affect sorption and desorption of PAHs in water as well as in simulated physiological gastric and intestinal conditions. Our model studies confirm that weathered nanoplastics can enhance the mobilization and bioaccessibility of PAHs and highlight the need for a systematic characterization of nanoplastics-associated accumulation of hydrophobic carcinogens in food chains.

RESULTS/DISCUSSION

Accelerated Plastic Weathering Model

Nanoplastics in marine ecosystems are categorized as primary or secondary nanoplastics depending on whether these materials are nanoscale by fabrication or the result of a weathering process of larger plastics debris, respectively. ^{16, 18} Secondary nanoplastics account for the bulk of the nanoplastics in marine ecosystems ^{16, 18} despite being the result of a relatively slow process that involves mechanical grinding through waves as well as photochemical weathering driven by incident sunlight. To emulate this natural plastic degradation process, we established an accelerated weathering protocol (**Figure S1**) that facilitates probing changes in the chemical properties of plastics at different stages of the weathering process without having to wait for months or even years, as in the case of the natural process.

In the first step of the weathering protocol, macroscopic consumer plastic objects selected to mirror the distribution of single-use plastics that disproportionately accumulate in the environment were shredded and milled to nanoscale size with the intent to determine if, as a mixture, plastics harbored pervasive chemical changes. The starting materials were comprised of common commodity plastics, including polyethylene terephthalate (PET), polypropylene (PP), low- and high-density polyethylene (LDPE and HDPE), polystyrene (PS), polyvinyl chloride (PVC), and acrylonitrile butadiene styrene (ABS) (for composition see **Figure S1A**).^{10, 16, 35, 36} X-ray Photoelectron Spectroscopy (XPS) of the nanoplastics generated by milling contained the carbon and oxidized carbon signals expected for polymeric materials, as well as trace signals related to zirconia (Zr) due to the use of Zr-coated beads in the milling process (**Figure S1C**, **Figure S2A**).

The nano-sized plastic particles generated through the milling process, which are referred to as 'native' nanoplastics throughout this manuscript, were introduced to simulated marine environmental conditions and exposed to a commercially available sunning-lamp containing ultra-violet (UV-A and UV-B) light for photochemical weathering, utilizing the accelerated weathering device and conditions described in the Methods section (**Figure S1A-F**). Key parameters of the UV weathering process, such as UV irradiance,

temperature, and salinity of the water were kept within the margins reported in previous accelerated weathering studies.^{37, 38} The nanoplastics were weathered for a total of 10 weeks, but samples were taken at weeks 0, 1, 2, 3, 4, 5, 8, and 10 to facilitate a continuous characterization of the weathering process.

Surface Morphology and Charge Characterization

Size and morphology of the nanoplastics were characterized by Scanning Electron Microscopy (SEM) and Dynamic Light Scattering (DLS). Due to the heterogeneity of the particles, approximately two thousand particles were selected at random from SEM images to measure their size along both the longest and shortest axis (Figure 1A). Both the short and long axis lengths for 'native' nanoplastics (no photochemical weathering) and 'weathered' nanoplastics (10 weeks maintained under UV-A, UV-B irradiation in sea water) nanoplastics show broad distributions. The short axis median lengths for native and weathered were 91 nm and 95 nm, respectively, and the short axis mean lengths were 154 nm and 161 nm. The long axis median lengths were 161 nm and 179 nm, and the long axis mean lengths were 282 nm, 304 nm. The number mean of the hydrodynamic diameter before and after UV irradiation of the particles as determined by DLS was 276 ± 104 nm and 251 ± 51 nm, respectively, with polydispersity indices of PDI = 0.46 ± 0.02 , 0.37 ± 0.20 (Figure 1B). Overall, these measurements indicate a nearly identical average size for the nanoplastics generated by milling before and after photochemical weathering.

To characterize changes in surface morphology associated with photochemical weathering, Brunauer–Emmett–Teller (BET) Isotherm measurements were performed. The isotherms revealed an increase in surface area by 73% but a decrease in average pore size by 37% at nearly constant pore volume (**Figure 1C**), indicating a roughening of the surface due to photochemical weathering. Next, to determine the impact of UV irradiation as a function of time on particle charge, zeta potential measurements were performed in de-ionized water (DI)³⁹ and ocean water (**Figure 1D**). As expected, the zeta potentials were more negative in DI than in ocean water due to a lack of positive counterions that can screen a more negative surface charge. Although more pronounced for DI water, for both DI and ocean water, the zeta potentials assumed their most negative value after 5 weeks of photochemical weathering and slightly increased afterwards.

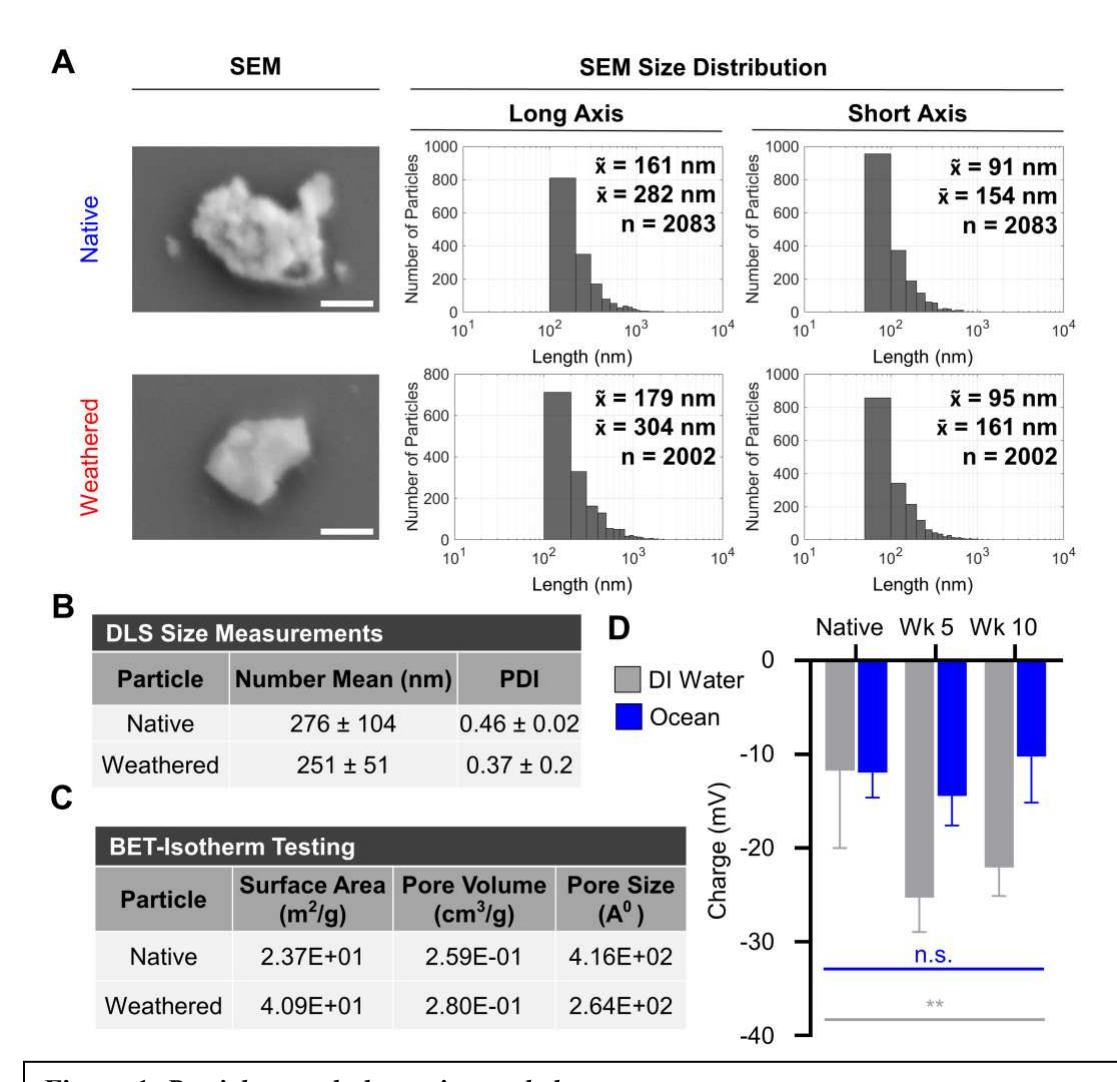


Figure 1. Particle morphology, size, and charge

187

188

189

190

- (A) Scanning electron microscope (SEM) images of nanoplastics before (native) and after weathering. Mean (\bar{x}, nm) , Median (\tilde{x}, nm) , and number of particles counted (n) reported for measurements along both the longest and shortest axis of each particle counted. Long and short axis measurements correspond to the same particle. Scale bar = 200 nm.
- **(B)** Dynamic Light Scattering (DLS) measurements for the number mean hydrodynamic diameter (nm) for native and weathered nanoplastics.
- (C) Brunauer–Emmett–Teller Isotherm (BET) reporting particle surface area (m²/g), pore volume (cm³/g), and Pore Size (A°) for native and week 5 weathered nanoplastics.
- **(D)** Zeta potential (meV) measurements for native, week 5, and week 10 nanoplastics. Error bars represent the mean \pm SD (n=3 independent weathering trials, with 3 repeated measurements). Kruskal-Wallis test was performed, **: p < 0.01, ns: p > 0.05.

The photo-fragmentation of plastics associated with the applied weathering protocol is also expected to affect the brittleness and other mechanical properties of the materials. Indeed, Differential Scanning Calorimetry (DSC) measurements confirmed a decrease in the

melting temperature and crystallization temperature, which is an indicator of a structural fragmentation of the nanoplastics (**Figure S2B**).

Vibrational Characterization of Nanoplastics

Infrared spectroscopy provides molecule-specific vibrational information and is therefore well suited to monitor the effect of photochemical weathering on the chemical composition of the nanoplastics during the accelerated weathering protocol applied in this work. Attenuated Total Reflection (ATR) Fourier Transform Infrared (FTIR) spectroscopy was performed with 2 mg of dry weathered nanoplastics collected at the aforementioned intervals. Transmittance spectra of native, as well as of 5 and 10 weeks weathered nanoplastics are shown in **Figure 2A**. The spectra exhibit pronounced changes as a function of weathering time. Peak assignments in **Figure 2A** are color-coded to match characteristic molecular features of potential PET fragmentation products as shown in **Figure 2B** (section [1]) as the following spectral analysis revealed that PET vibrational features dominate the spectra.

The broad band at 3357 cm⁻¹ in the spectra of the native nanoplastics suggests that -OH groups are present in the native nanoplastics, perhaps as a result of surface oxidation or contamination of byproducts found in recycled plastics.⁴⁰ The features at 2915 cm⁻¹ and 2850 cm⁻¹ are characteristic of C-H vibrational modes in aliphatic segments (**Figure 2A**).⁴¹ The band at 1716 cm⁻¹ designates carbonyl groups in PET, and bands at 1556 cm⁻¹, 1262 cm⁻¹, and 1098 cm⁻¹ are associated with benzene ring stretching and bending modes along the PET chain.⁴¹⁻⁴⁶ The feature at 723 cm⁻¹ is assigned to the C-H out of plane wagging mode on the para functionalized aromatic ring of PET.^{43, 44} A comparison of the native spectrum to the Thermo Fisher OMNIC spectrum libraries, as described in the Methods, identifies PET as key component in the mixture (**Figure S3A**). For a complete list of peak assignments for the spectra, please refer to **Supporting Information Table 1**.

Although the nanoplastics were generated as a mixture of different plastics, many of the dominating spectral features can be assigned to PET. The high intensity of PET-associated signals is likely related to intrinsic cross-sections of the molecular vibrations related to PET. C=O stretching modes of carbonyl groups and benzene ring bending modes are

known to give rise to strong to very strong band intensities in PET.⁴¹ With regard to the other plastics, we may have expected more signal from PVC due to the bound chlorine, which gives rise to some polarity. However, when investigating nanoplastics generated from plastics samples not-containing PET as a starting material (**Figure S3,B-E**), this mode was not very pronounced (**Figure S3B**). Given the less polar functional groups of the other plastics materials, it is perhaps unsurprising that PET features dominate in the PET containing mixture (**Figure 2A**).

The spectra of nanoplastics weathered for 5 weeks contain many of the same bands as found in the native nanoplastics spectra. While most vibrational features show an increase in transmittance (decreased intensity), such as 1716 cm⁻¹, 1245 cm⁻¹, 1100 cm⁻¹, and 723 cm⁻¹, the broad -OH band at 3,357 cm⁻¹ shows a strong drop in transmittance (increased intensity), indicating an increase in hydroxyl groups. Furthermore, a new band emerges in the C=O range at 1,637 cm⁻¹, which may indicate the formation of quinones, benzophenones, or carboxylic acids as degradation products of PET under UV irradiation (**Figure 2A,B**). ^{35, 43} Additional potential degradation products are summarized in **Figure S3F**. ^{35, 43}

Spectra recorded after 10 weeks of weathering contain obvious spectral differences when compared to the spectra of native nanoplastics or the week 5 measurement. In particular, new bands are detected at, in order of contribution: 1400-1500 cm⁻¹, 873 cm⁻¹, 712 cm⁻¹, 2513 cm⁻¹, 1790 cm⁻¹ (**Figure 2A,B**). This combination and intensity of bands is characteristic of calcium carbonate (**Figure S3G**).^{42, 47} The FTIR spectra are consistent with a degradation process that results in the release of CO₂, a product of the photo-oxidation of PET under oxygen-rich conditions.³⁵ CO₂ release leads to the formation of carbonate ions in water, which in the presence of Ca²⁺ ions in seawater causes the deposition of poorly soluble CaCO₃ [13 mg/L]^{48, 49} on the plastic nanoparticles (**Figure 2B**, section [2]). This hypothesis is corroborated by the fact that nanoplastics photochemically weathered in calcium-depleted seawater or DI water do not show any indications of CaCO₃ deposition (**Figure S4,A-D**), which is likely due to an increased solubility of CO₃²⁻ in the absence of Ca²⁺. XPS spectra of nanoplastics photochemically weathered in ocean water

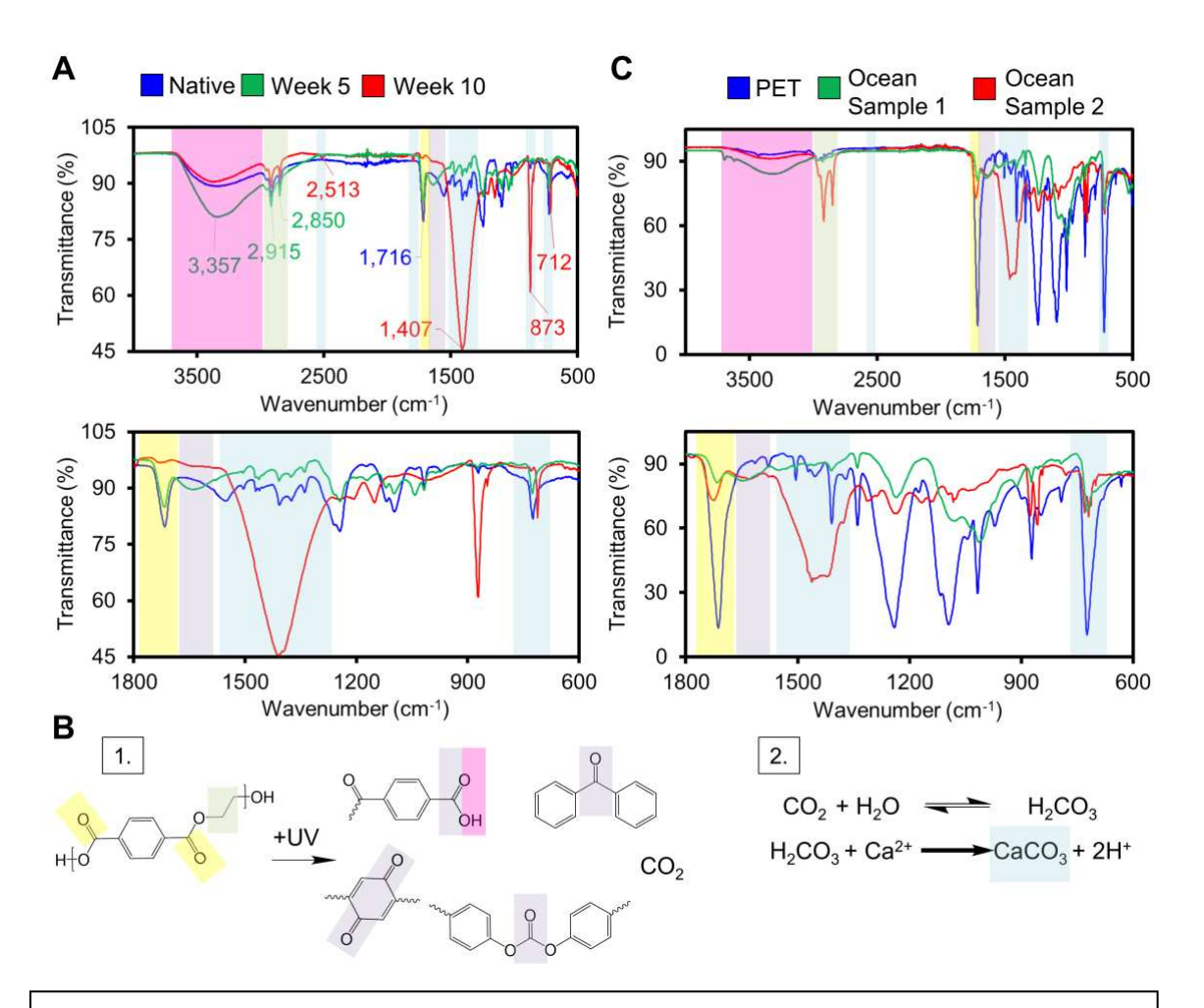


Figure 2. Effect of photchemical weathering on FTIR spectra of nanoplastics

- **(A)** Fourier-Transform Infrared Spectroscopy (FTIR) spectra for native and post 10 weeks of weathering nanoplastics. The top spectrum covers the wavenumber range 500 to 4000 cm⁻¹ and the bottom the spectral range 600 to 1800 cm⁻¹.
- **(B)** PET plastic and known degradation products [1] and postulated reactions of released CO₂ in ocean water [2]. Color coding in [1] and [2] corresponds to spectral bands in (A) and (B).
- (C) Fourier-Transform Infrared Spectroscopy (FTIR) spectra for an unweathered PET plastic bottle from 1985 and PET plastic bottle (Sample 1) and unknown plastic (Sample 2) harvested off the coast of Hawaii. The top spectrum covers the wavenumber range 500 to 4000 cm⁻¹ and the bottom the spectral range 600 to 1800 cm⁻¹.

for 10 weeks provide additional evidence of calcium carbonate deposition. The Ca 2p_{3/2}-2p_{1/2} splitting at 3.5 eV is characteristic of calcium carbonate⁵⁰; this splitting is not observed for native plastics (**Figure S4E**). Interestingly, SEM images of larger plastics particles show a rougher surface morphology for weathered plastics, which may be partially caused by crystal deposition on the particles as they resemble calcite crystal structures (**Figure S4F**).⁵¹ Deposition of charge-neutral CaCO₃ on nanoplastics surfaces may also account for the slight increase in zeta potential observed between samples weathered for 5 and 10

weeks (**Figure 1D**). Moreover, MP-AES revealed an approximately 20-fold higher Ca²⁺ content for nanoplastics after 10 weeks of photochemical weathering than for native nanoplastics or compared to nanoplastics not containing PET as a starting constituent weathered for 10 weeks (**Figure S5A**). Likewise, FTIR spectra of weathered plastics mixture devoid of PET did not contain any spectral signatures indicative of CaCO₃ (**Figure S3B**). In addition to photochemical weathering experiments, control experiments were performed that maintained nanoplastics samples in sea water in the dark under otherwise identical conditions (**Figure S5B**). The spectra of these controls indicate little to no degradation and show no CaCO₃ deposition, confirming that the observed changes in **Figure 2A** are primarily the result of UV-light induced photodegradation. These findings suggest that under the chosen experimental conditions, PET degradation is the main source of CO₂ and that CO₂ release is responsible for the carbonate deposition.

The release of CO₂ from PET as a result of photodegradation may be accompanied by the release of other degradation products, such as polymer monomers and oligomers, or other chemicals associated with commercial plastic production into the surrounding water. We therefore analyzed the filtrate, i.e. the ocean water obtained after collection of nanoplastics through filtration as seen in **Figure S1F**, of an independent weathering experiment of PET through GC-MS. Consistent with the proposed photodegradation mechanism, we observed traces of bisphenol A (BPA), terephthalic acid (TPA), and benzoic acid (BA), which are known starting materials or byproducts associated with PET degradation (**Figure S5C**).⁴³, 44, 46

The spectra obtained with the accelerated weathering protocol are in general agreement with previously published spectra of nanoplastics from the ocean.^{35, 46, 52} FTIR spectra of a PET bottle (Ocean Sample 1) collected from the Pacific Ocean as well as from a pristine (i.e. not exposed to environmental weathering) PET bottle are included in **Figure 2C**. Several spectral features of the accelerated weathering sample show similar trends as observed in the ocean sample. In particular, the decreased intensities (increased transmittance) at 1716 cm⁻¹, 1245 cm⁻¹, 1100 cm⁻¹, and 723 cm⁻¹ and the increase in intensity (decreased transmittance) at 3357 cm⁻¹ for week 5 of accelerated weathering mirror intensity changes observed in 'Ocean Sample 1' (**Figure 2A,C**).⁴⁶ Another unknown

sample collected in the ocean, referred to 'Ocean Sample 2' (**Figure 2C**), shows a pronounced and broad feature in the 1400-1500 cm⁻¹ range, indicative of CO₃²⁻ deposition as observed for the accelerated weathering protocol (**Figure 2C**). Other weaker CO₃²⁻ related features at 873 cm⁻¹ and 712 cm⁻¹ shared by Ocean Sample 2 and the accelerated weathering sample (week 10) can also be attributed to carbonate deposition.

Spectral Analysis by PCA and Machine Learning Models.

To further characterize the spectral changes associated with photochemical weathering and to classify the recorded data, Principal Component Analysis (PCA) was performed. The scores for the first three principal components (PCs) that together describe 98% of the total variance (Figure S6A) of the FTIR data set are plotted for 10 spectra per weathering condition (Figure 3A). The spectra for the different irradiation times cluster in distinct regions of the PC1-3 space. The clusters for weeks 0 (native) - week 2 separate along PC2, but starting from week 3, a separation along PC3 sets in. The measurements for weeks 3 and 4 cluster together but are clearly separated along PC3 from the spectra recorded in weeks 5, 8, and 10. The loading spectra of PC2 and PC3 provide information about the vibrational features that contribute most to the observed changes in PC space (Figure 3B). In the PC2 loading spectrum, the bands associated with PET degradation dominate, decreases in intensity (increased transmittance) 1716 cm⁻¹, 1245 cm⁻¹, 1100 cm⁻¹, 873 cm⁻¹ ¹, and 723 cm⁻¹ and an increase in intensity (decreased transmittance) at 3357 cm⁻¹, are observed, while the PC3 loading scores contain strong contributions from vibrational bands associated with CaCO₃, in order of contribution: 1400-1500 cm⁻¹, 873 cm⁻¹, 712 cm⁻¹, 2513 cm⁻¹, 1790 cm⁻¹. Importantly, the sign of the loading scores matches that of the change in transmission associated with weathering (Figure 3B, Figure 2A).

PCA is an unsupervised exploratory data analysis strategy. The classification of the data can potentially be improved using a supervised classification strategy. Inspired by the conventional carbonyl index as a starting point of our analysis, ^{46,53} we permutated over the transmittance ratios for all possible wavenumber pairs and determined which combination achieved the best separation of the individual accelerated weathering conditions. This analysis revealed that the combination of wavenumbers 1424 cm⁻¹ (CaCO₃) and 1722 cm⁻¹ (PET C=O) achieves the greatest separation amongst the different weathering times,

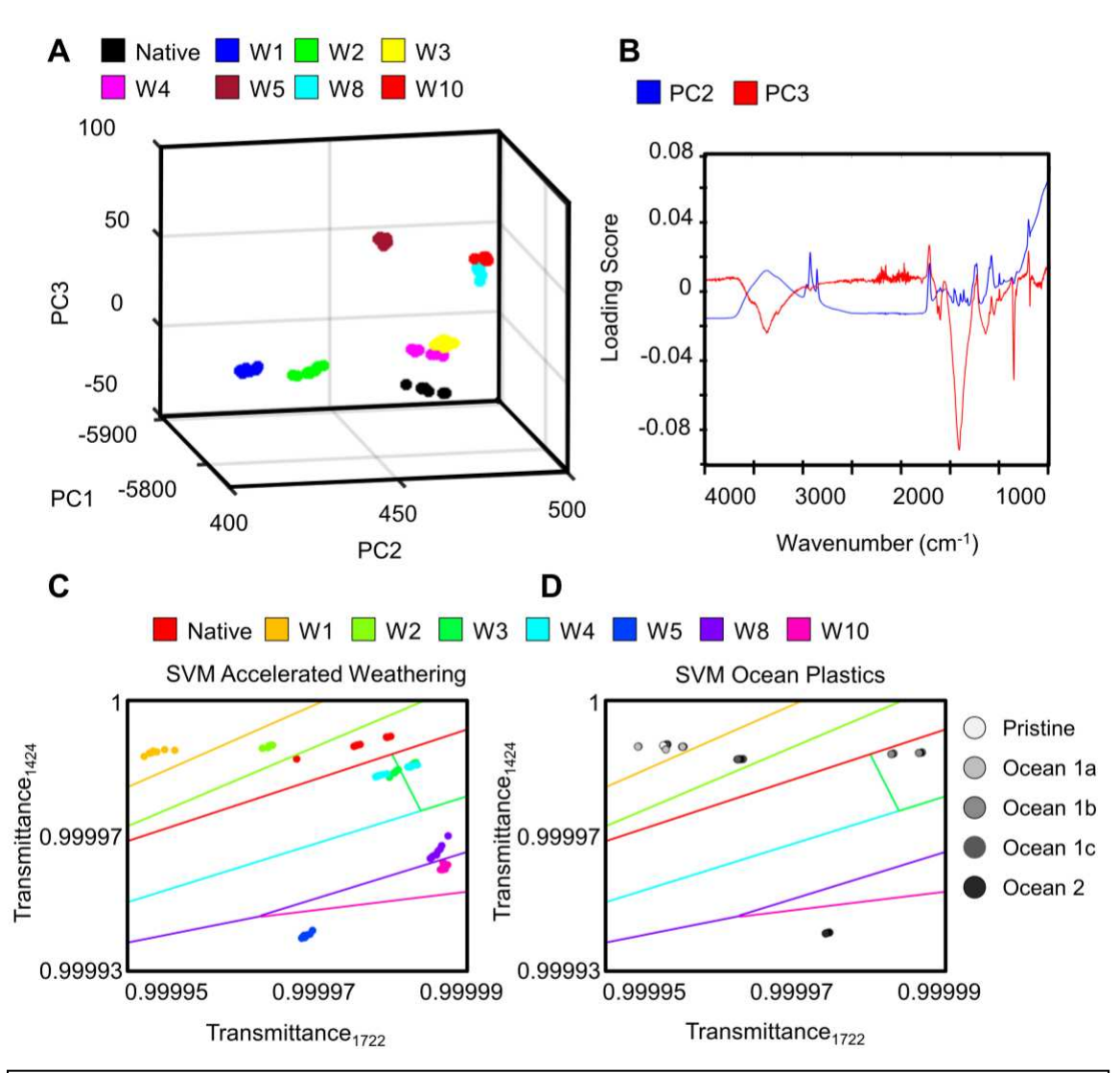


Figure 3. Characterization of nanoplastics before and after photochemical weathering

(A) 3D plot of Principle Component 1 vs. Component 2 vs. Component 3 for native and nanoplastics after photochemical weathering for 1, 2, 3, 4, 5, 8, and 10 weeks.

(B) PCA loading scores as a function of wavenumber (cm⁻¹) for principal components 2 and 3.

(C) Support Vector Machine (SVM) linear discriminant model training boundaries overlaid on transmittance at 1424 cm⁻¹ wavenumber vs. transmittance at 1722 cm⁻¹ wavenumber values for

(D) SVM model from Figure 3C overlaid onto intensities for ocean plastics.

the 10 samples per native, weeks 1-5, 8, 10 groups.

consistent with our model that degradation of PET and release of CO₂ results in the deposition of CaCO₃ onto the nanoplastics. In the next step, FTIR spectra were normalized by the integrated transmittance (from **Figure 2A**), and Support Vector Machine (SVM) models were fit to all spectral information for all weathering conditions as training set. A linear discriminant SVM model (**Figure 3C**) was found to best explain our data with over 95% accuracy (**Figure S6B**). The boundaries of the SVM model projected onto the 1424

cm⁻¹, 1722 cm⁻¹ transmittance sub-space are denoted by the continuous lines in **Figure 3C**.

The experimental data points (10 measurements for native, weeks 1-5, 8, and 10) cluster

furthest apart and accurately in regions defined by these boundaries, suggesting that 1424

cm⁻¹, 1722 cm⁻¹ define features that play key roles in the best performing SVM model.

In **Figure 3D** the SVM model was applied to classify FTIR spectra (**Figure S6C**) of macroscopic plastic samples collected from the ocean and a pristine control that is at least as old as the ocean samples. The pristine PET bottle was classified as sample weathered for 1 week, 'Ocean Sample 1' and similar PET bottles (Ocean Samples 1a-c), which are devoid of any vibrational carbonate signals, were classified as samples weathered for 1-4 weeks, and finally Ocean Sample 2 that shows clear carbonate signatures was classified as plastics sample weathered for 5-10 weeks. The classification model derived from nanoplastics generated by accelerated weathering in the laboratory successfully distinguishes between the investigated ocean plastics samples and attributes differences to increasing weathering durations.

PAH Sorption and Bioaccessibility

Changes in the chemical surface properties of nanoplastics over the course of photochemical weathering may affect the sorption of hydrophobic molecules. ^{10, 36, 54, 55} Indeed, stimulated emission depletion (STED) microscopy fluorescent dyes and Rose Bengal hydrophobicity assays indicated a loss in nanoplastics hydrophobicity due to weathering (**Supporting Information and Figure S7**). The effect of these surface changes on sorption and desorption of selected PAHs is characterized in the following. We chose benz[a]anthracene (molecular weight MW = 228), benzo[a]pyrene (MW = 252), and indeno[1,2,3-c,d]pyrene (MW = 276) for this study as these molecules are the best characterized PAHs and all three are cancerogenic. ⁵⁶ Incubating nanoplastics in an aqueous environment with a constant concentration of PAHs for an extended period of time most closely resembles the sorption process in nature. To experimentally realize this strategy, PAH-loaded inert silicon matrices were applied as PAH reservoirs that establish a constant, solubility-limited PAH concentration in an aqueous milieu. Nanoplastics were 'passively' loaded in this fashion by incubation for up to 60 days (**Figure S8A**). The PAH concentration (benz[a]anthracene) associated with the nanoplastics gradually increased

throughout the duration of the experiment, confirming that nanoplastics accumulate PAHs as function of time in aqueous media containing low concentrations of the hydrophobic compounds. However, due to the slow kinetics of the passive loading strategy, this approach was not the method of choice for systematically evaluating the sorption and desorption of PAHs to / from nanoplastics exposed to different weathering conditions. Instead, nanoplastics were loaded in this work by incubating 1 mg nanoparticles in 1 mL of a 50 : 50 methanol: water mix containing 50 µg PAH per mL for up to three days. This approach resulted in PAH concentrations that were 33% higher than those obtained with the passive loading after 2 months. One potential concern is that the methanol: water mix may affect the nanoplastics chemistry and interfere with the surface properties generated by the weathering process. FTIR spectra and XPS spectra of native, week 5, and week 10 weathered nanoplastics samples exposed to a 50 : 50 methanol : water mix for 3 days did not, however, show pronounced differences to those of the original nanoplastics, ruling out systematic changes in the nanoplastics chemistry (**Figure S8B-D**).

All PAHs were found to sorb to both native and weathered plastics to a high degree (Figure 4A, for additional loading time points see Figure S9A). Significant differences in PAH sorption were only detected between native nanoplastics and nanoplastics weathered for 5 or 10 weeks in the case of Benz[a]anthracene. In order of increasing weathering time (native, week 5, and week 10) the sorbed concentrations were 1.695±0.537, 1.275±0.546, 1.128 ± 0.407 µg/mg of nanoplastics for Benz[a]anthracene $> 0.570\pm0.427$, 0.213 ± 0.130 , 0.213 ± 0.133 µg/mg of nanoplastics for Indeno[1,2,3-c,d]pyrene > 0.0767 ± 0.0462 , 0.0379±0.0208, 0.0375±0.0250 µg/mg of nanoplastics for Benzo[a]pyrene. PAH sorption was overall higher for native nanoplastics than for weathered plastics, but both native and weathered plastics have significant capacity as potential vector for PAHs. In both cases, the nanoplastics-associated PAH concentrations were approximately a factor of 1000 higher than the aqueous solubility of the PAHs.⁵⁷ PAH sorption was also investigated on mixtures devoid of PET (Figure S1A). It was determined that the loading capacity of the mixture devoid of PET (Figure S9B) is greater than that of mixtures containing PET by a factor of 4.8-7.4 depending on the PAH. This observation can be rationalized by the fact that the other plastics components are less polar than PET, yielding a more hydrophobicfriendly environment.

To evaluate the potential effect of nanoplastics on PAH bioaccessibility, we characterized PAH desorption from native and weathered (5 and 10 weeks) nanoplastics in water as well as under simulated physiological conditions. To that end, PAH-loaded nanoplastics were incubated in gastric juices for 0.5, 1.5, and 3.5 hours or in intestinal fluids for 1, 4, and 8 hours to emulate realistic exposure times.^{58, 59} The compositions of the simulated gastric iuices and intestinal fluids used in this work are listed in Supporting Information Table 2. PAH desorption was measured by quantifying the difference in PAH associated with the nanoplastics before and after incubation relative to that of nanoplastics incubated in equivalent volumes of DI water. No significant difference between the different incubation times in gastric juices and intestinal fluids was discovered (Figure S10A,B), only the end points are shown in **Figure 4B,C**. Exposure to simulated gastric juices of the stomach increased the desorption of PAHs by 2.30-23.55% for Benz[a]anthracene, 43.44-59.74% for Benzo[a]pyrene, and 21.30-42.31% for Indeno[1,2,3-c,d]pyrene (Figure 4B). Interestingly, in the case of Benz[a]anthracene and Benzo[a]pyrene, weathered nanoparticles showed more desorption than native nanoplastics, indicating that nanoplastics weathering favors PAH desorption in gastric juices.

Incubation in intestinal fluids also enhanced PAH desorption; the desorption was enhanced by 18.69-43.80% for Benz[a]anthracene, 15.67-53.69% for Benzo[a]pyrene, and 75.63-88.34% for Indeno[1,2,3-c,d]pyrene (**Figure 4C**). For all PAHs, desorption from native plastics was higher for small intestine conditions than for gastric conditions, which we attribute to the fact that stomach acids are less effective at solubilizing hydrophobic PAHs than intestinal fluids, whose bile contains amphiphilic lipids and other factors that can act as surfactant and solubilize hydrophobic compounds. However, unlike in the case of the gastric juices, weathering decreased the desorption of PAHs from nanoplastics in intestinal fluids. One possible explanation may be that changes in the surface properties induced by weathering result in decreased interactions between the sorbed PAHs and solubilizing components of the intestinal fluids.

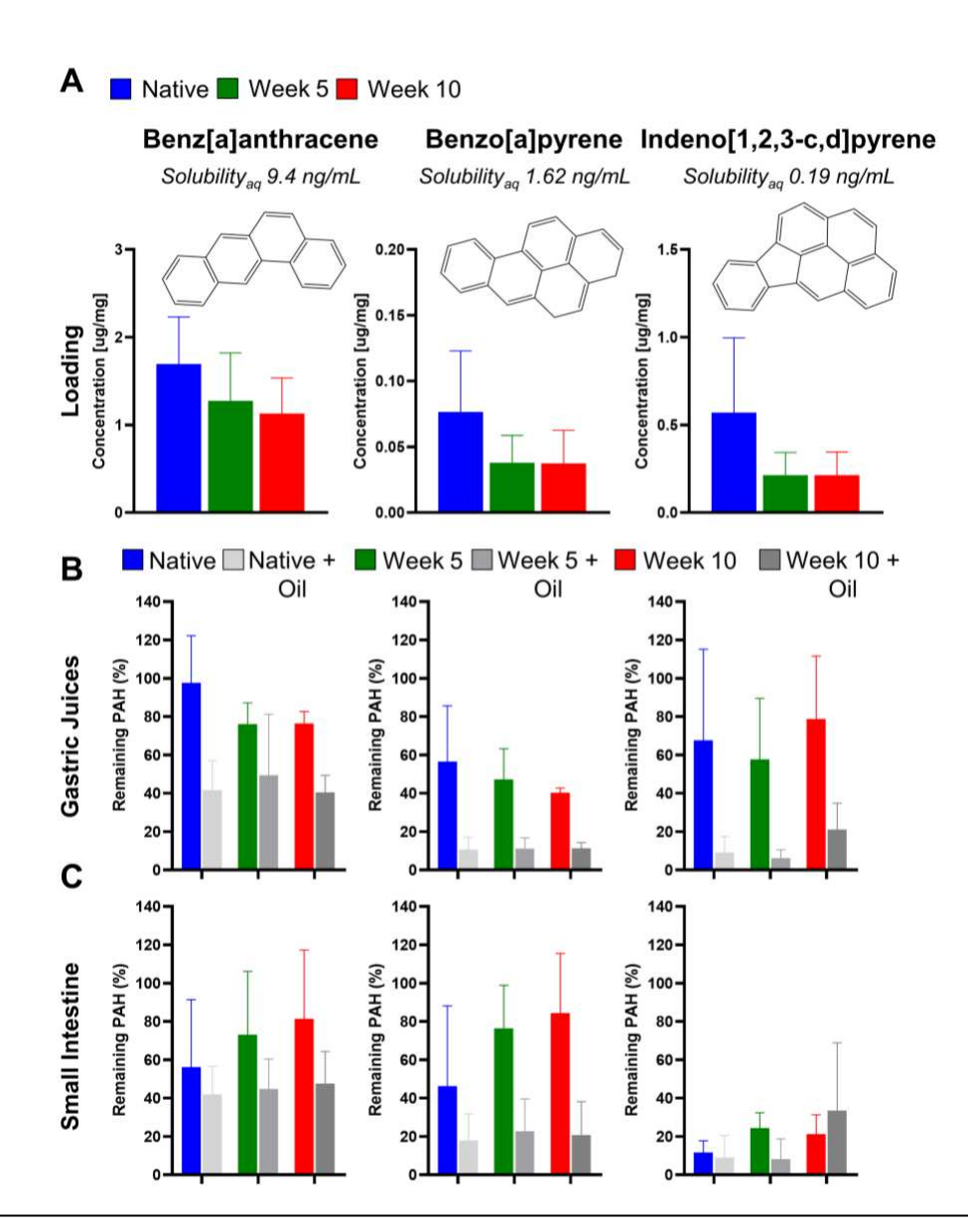


Figure 4. PAH Loading and Bioacessibility

426

427 428

- (A) PAH concentration in ug per mg of nanoplastics for native, nanoplastics after photochemical weathering for 5 and 10 weeks. Published aqueous solubilities of respective PAHs are shown as a function of ng PAH per 1 mL of solvent, n = 10.
- **(B)** Percent of PAHs released from native and nanoplastics after photochemical weathering for 5 and 10 weeks as function of exposure to gastric juices with and without the presence of hydrophobic olive oil. Percentages are with respect to nanoplastics incubated within equivalent volumes of deionized water, n = 8.
- (C) Percent of PAHs released from native and nanoplastics after photochemical weathering for 5 and 10 weeks as function of exposure to intestinal juices with and without the presence of hydrophobic olive oil. Percentages are with respect to nanoplastics incubated within equivalent volumes of deionized water. Statistics for a-c can be found in **Supporting Information Table** 3. Error bars represent the mean \pm SD (n = 8).

Another factor that may impact the bioaccessibility of PAH-loaded nanoplastics is food ingested together with PAH-containing nanoplastics. Especially fat-rich food is expected to affect the desorption of PAHs. This was tested by adding 2 mL (8% by volume) olive oil to the gastric juices or intestinal fluids.^{60, 61} The addition of the oil resulted in a massive decrease of PAHs bound to nanoplastics, resulting in an increase of PAH desorption by 51-92%, confirming that fatty foods have a potential for substantially increasing the bioaccessibility of nanoplastics-associated PAHs (**Figure 4B,C**).

436437

438

439

440

441

442

443

444

445

446

447

448

449

450

451

452

453

454

455

456

457

458

459

460

461

430

431

432

433

434

435

CONCLUSIONS

We have shown that nanoplastics experiences tractable morphological and chemical changes under accelerated photochemical weathering conditions that mimic photodegradation processes in the ocean. CO₂ is released from PET-containing plastics during photodegradation, resulting in the deposition of CaCO₃ on nanoplastics. Machine learning models developed from FTIR spectra of nanoplastics exposed to the accelerated weathering protocol under defined conditions successfully distinguished and classified different plastics samples collected from the ocean. The ability to classify unknown plastics samples is of interest for recycling efforts, which require sorting based on composition. Importantly, not all CO₂ released during plastics weathering is converted to CaCO₃ and thus plastics debris could represent a long-time source for CO₂ greenhouse gas emission. Given the large amount of plastics debris in the ocean, this point requires further investigation to quantify the potential effect. The recorded PAH sorption and desorption data show that despite photochemical weathering and CaCO₃ deposition, nanoplastics effectively serve as sponges for hydrophobic compounds such as PAHs, which are known to increase the risk of cancer. These findings demonstrate that the assessment of detrimental health effects associated with nanoplastics need not only be investigated with respect to direct effects, but also in context of indirect risk factors, such as the ability to mobilize carcinogens into the food chain^{16, 36} and subsequently into humans. Further studies are warranted to investigate nanoplastics weathering on a single particle level to determine the extent and frequency to which weathering impacts the formation or release of oligomers, monomers, and other potential chemicals from nanoplastics as a function of weathering. This information would be desirable to characterize the molecular mechanism of the nanoplastics photodegradation.

METHODS/EXPERIMENTAL

463

462

464 Ocean Water

- Ocean water that was collected from Coast Guard Beach, Massachusetts, 41.8435° N,
- 466 69.9482° W and filtered using an 100 nm vacuum filter flask (Nalgene, catalog no. 568-
- 467 0010).

468

469

Plastics from Pacific Ocean

- Plastics were a generous gift from Sustainable Coastlines Hawaii, facilitated by Rebecca
- 471 Mattos. The plastics were harvested by representatives from Sustainable Coastlines
- Hawaii, Sea Cleaners New Zealand, and Nā Kama Kaiha at Kahuku Beach on O'ahu,
- 473 coordinates 21°40'48.1"N 157°56'30.8"W.

474

475

Plastic Sample Preparation and Weathering

- 476 Plastics collected from everyday household items, including a Ziploc bag (LDPE),
- Tupperware container (PP), Starbuck's single-use cup (PP), and Poland Spring single-use
- water bottle (PET), Solo Cup (PS), Pipe (PVC), Foam Container (PS), Computer case
- 479 (ABS), and container (HDPE) were utilized for this study as a function of mass input
- 480 (Figure S1A). The plastics were suspended in water and broken up using an everyday
- household blender, made by Hamilton Beach (Figure S1B). Plastics were then suspended
- in 25 mL of water and approximately 15 cm³ worth of 0.3 mm diameter YSZ balls (catalog
- 483 no. 4039GM-S003, Inframat). This cocktail was placed in a Semi-Clear HDPE Plastic Vial
- 484 (catalog no. 4280T31, McMaster-Carr) and milled using standard workshop ball mill for
- 485 10x 15 minutes on 5 minutes off intervals (Figure S1C). To remove the YSZ balls, the
- cocktail was filtered through an Advantech L3-S100 Standard Sieve, Stainless Steel Mesh,
- 487 0.150 mm sieve (catalog no. EW-59948-41). Plastics were then filtered through a 100 nm
- 488 filter (catalog no. 568-0010, Thermo Fisher Scientific). The cocktail was washed with
- water by centrifugation, 2x10 mins at ~4600 G (5000 rpm). Plastics were re-suspended in
- 490 3.5 L of ocean water. Using a 160 Watt Lucky Herp Reptile UVA/UVB Mercury Vapor
- Bulb (catalog no. R115, Lucky Herp) emitting 1560 uW/cm² UVB from a distance of 30
- cm on center, the plastics were treated with artificial sunlight at intervals of 4 hours on and
- 6 hours off to mirror sunlight cycles and to keep the water temperature under 45°C (**Figure**

S1D-E). To mimic the movement of ocean water and to ensure plastics received exposure to air in some capacity, the 3.5 L cocktail was simultaneously stirred using a standard magnetic stir bar and plate setup. Evaporated ocean water was replenished with deionized water once per day to ensure that the salt content remained stable and to better control the temperature of the reaction vessel. At designated intervals, portions of the plastics were filtered out using a 100 nm filter to be later used for analysis (**Figure S1F**). Plastics were spun down using centrifugation and dried overnight. Samples were stored at room temperature in the dark.

502

503

504

505

506

507

508

509

510

511

512

513

514

515

516

517

518

519

520

521

494

495

496

497

498

499

500

501

SEM Sample Preparation and Imaging

Silicon wafers (catalog no. 809, University Wafer) were cut, placed in ethanol, and sonicated for 5 minutes in order to remove contaminants and debris. Wafers were then dried under vacuum overnight. Nanoplastics were suspended in DI and then drop coated onto the silicon wafers. The dilution of nanoplastics varied between 10-100 [µg/ml] in order to optimally disperse nanoplastics and reduce agglomeration. Importantly, all time points (native, weeks 1-5, 8, 10) for a given trial utilized the same concentration of nanoplastics. After drop coating, wafers were placed under vacuum overnight to dry samples completely. Samples were sputter coated with gold/palladium for 15 seconds under argon in order to minimize particle charging. Imaging was performed using a Zeiss SUPRA 55-VP scanning electron microscope (SEM) with parameters EHT 3.0 keV, 20 µm Aperature, 'SE2' and 'InLens' mixed signal mode. The working distance was adjusted as necessary. To determine average nanoparticle sizes, measurements were performed in the center of the drop coated sample, spatially well separated away from the peripheral "coffee ring" in order to avoid aggregates. Images were taken at 15,000x and nanoplastics counts and dimensions were determined using an in house written Matlab (The Mathworks Inc., Natick, MA) script. Briefly, images were binarized, which created a background with the color black and objects with the color white. The longest axis and shortest axis of each object was determined, creating a bounding box. Bounding boxes were counted and plotted in a histogram as a function of long and short axis length.

522523

524

DLS measurements for hydrodynamic diameter and Zeta Potential

Size and zeta potential measurements were determined by using Zetasizer Nano ZS90

526 (Malvern, Worcestershire, UK). To measure the size of NPs, Deionoized water and ocean

water was used to dilute the NPs.

528

529

527

BET-Isotherm Testing

- Native nanoplastics and Week 5 nanoplastics were harvested and sent to Micromeritics
- company and were analyzed using a Physi-13 profile, which allowed for High-resolution
- micropore analysis plus mesopore isotherm (4 Å to 3000 Å).

533

534

Fourier-transform Infrared Spectroscopy, Principal Component Analysis, Support

- 535 Vector Machines
- Nanoplastics were filtered as above and dried under vacuum overnight in preparation for
- analysis on a Nicolet Nexus 670 FTIR with Attenuated total reflection (ATR). Using a
- razor blade, 2mg of nanoplastics were scraped onto the diamond ATR and compressed.
- Data were collected using a DTGS KBr detector, KBr Beam Splitter, Range 4000 to 400,
- optical velocity 0.6329, Aperature 34. Thermo Fisher lookup library was comprised of data
- sets from 'Aldrich Condensed Phase Sample Library', 'Aldrich Vapor Phase Sample
- 542 Library', 'Georgia State Crime Lab Sample Library', 'HR Thermo Nicolet Sample
- 543 Library', 'Hummel Polymer Sample Library', 'Nicolet Condensed Phase Academic
- Sampler Library', 'Organics by RAMAN Sample Library', and 'Sigma Biological Sample
- Library'. Principle component analysis and 3D plots were performed using in house Matlab
- scripts. Support vector machine investigations were performed using both the classifier
- learner app published by Matlab as well as with a combination of in-house scripts. Fitting
- the complete data set to a total of thirty-two SVM models revealed the linear discriminant
- model best described our data.

550551

Differential Scanning Calorimetry (DSC)

- Nanoplastics were dried under vacuum as above. Nanoplastics were placed into a 40 µL
- crucible (catalog no. 11A16017, Thermal Support) and referenced using Indium.
- Parameters include: 40 °C start temp, 300 °C end temp, 10 °C/min heating rate, Argon
- 555 Segment Gas

557 Microwave Plasma Atomic Emission Spectroscopy (MP-AES)

- Samples were dissolved in 2% HNO₃ acid (catalog no. A200-212, Fisher Scientific)
- recommended by Agilent (Santa Clara, CA) on an Agilent Technologies 4200 MP-AES
- instrument. Calcium chloride (catalog no. C3881-500G, Sigma-Aldrich) was used for
- generating the standard curve. Parameters include: 3 replicates, 15 rpm peristatic pump
- speed, 45s uptake time, 30s rinse time, 15s stabilization time, and 7 pixels.

563

564

X-ray Photoelectron Spectroscopy (XPS)

- X-ray photoelectron spectroscopy was performed using a Nexus K alpha instrument.
- Samples were drop coated onto a silicon wafer as above and let to dry under vacuum for
- 567 24 hours. Investigation of elements composition was determined using the survey scan
- function. To determine oxidation states over these sample, we performed a high-resolution
- OS1, C1S, and Ca2p scans. Plots utilized background correction called 'Smart'
- 570 background.

571

572

Filtrate Studies

- 573 1.5L of the total 3.5L filtrate volume was collected at week 10 and rotovapped down to a
- volume of 100mL. Due to the high concentration of precipitated salt, we centrifuged the
- sample at 4,500 G. The supernatant was removed and mixed as a 50 : 50 solution with
- acetonitrile. The sample was then analyzed by Gas Chromatography-Mass Spectrometry
- 577 (Agilent 6890N GC-MS, Agilent 7683B Sampler, 5.0 µL syringe catalog no. 5188-5246,
- and am Agilent J&W ZB-5msplus Ultra Inert 30 m × 0.25 mm, 0.25 µm column catalog
- 579 no.7HG-G030-11). Spectra were compared against standards and the Agilent MS database.

580

581

Silicone Wafer Passive PAH Loading and Analysis

- PAH's were purchased from Sigma Aldrich: Benz[a]anthracene (catalog no. 48563),
- Benzo[a]pyrene (catalog no. 51968-50MG), Indeno[1,2,3-cd]pyrene (catalog no. 94377-
- 584 10MG). For passive loading, platinum Cured Silicone sheets (.040"+/-0.002" thickness,
- Interstate Specialty Products, catalog no. 37604) were punched with a standard 3 ring hole
- punch. Loading of PAH's were established according to previous studies with slight
- modification. 62 Briefly, these disks were introduced to methanol containing PAH's above
- saturation levels to create a reservoir of PAH. Disks were loaded with PAHs for 72 hr at

589 room temperature on a shaker. The disks were then removed from the loading solution and 590 were wiped with paper towel. Finally, they were rinsed three times for 1 hr each with 591 Deionized water to remove any residual methanol and free PAH. 1mg of Nanoplastics were 592 suspended in 1 mL of DI water and 1 silicone wafer was added to each solution. For 593 analysis, wafers were removed, and the nanoplastics were spun down. The aqueous 594 supernatant was removed and particles were resupended in dichloromethane (DCM). 595 Nanoplastic solutions were placed on the shaker overnight to extract PAHs from the 596 nanoplatics. The next day, 250 µL of DCM was then transferred to vials (Agilent, catalog 597 no. 5188-6592, 5182-0724) and were analyzed using Gas Chromatography-Mass 598 Spectrometry (Agilent 6890N GC-MS, Agilent 7683B Sampler, 5.0 µL syringe catalog no. 599 5188-5246, and am Agilent J&W ZB-5msplus Ultra Inert 30 m × 0.25 mm, 0.25 µm 600 column catalog no.7HG-G030-11). Parameters included: 1.0 µL splitless injection, 601 Carrier: Helium 45 cm/s, constant flow, Inlet: Pulsed splitless; 300 °C, 40 psi until 0.2 602 min, purge flow 30 mL/min at 0.75 min, Oven: 55 °C (1 min) to 320 °C (25 °C/min), hold 603 3 min, Detection: MSD source at 300 °C, quadrupole at 180 °C, transfer line at 280 °C, 604 scan range 45 to 450 AMU.

605

606

Methanol: DI water Loading and Analysis

- Nanoplastics were suspended in 1mg/mL of DI water: Methanol Mix containing
- Benz[a]anthracene [25 $\mu g/mL$], Benzo[a]pyrene [25 $\mu g/mL$], and
- Indeno[1,2,3-cd]pyrene [25 $\mu g/mL$] into Eppendorf tubes were shaken for various intervals
- 610 to determine the optimal loading time. Solutions were spun down and the supernatant was
- removed. PAH extraction and analysis was performed as above.

612

613

PAH Desorption Profiles

- 1 mg of PAH loaded nanoparticles were suspended into 25 mL of deionized water, gastric
- 615 juices master mix, or intestinal juices master mix. Master mixes were formulated according
- 616 to the literature.⁵⁸ Briefly, 'Gastric Juice Mastermix' composed of 100 mg of urea (catalog
- 617 no. U5378-1KG, Sigma Aldrich), 200 mg of D-Glucuronic acid (catalog no. G5269-10G,
- 618 Sigma Aldrich), 122 mg of sodium phosphate dibasic (catalog no. S3264-1KG, Sigma
- Aldrich), 317 mg of ammonium phosphate (catalog no. A3048-500G, Sigma Aldrich), 350
- mg of glucosamine hydrochloride (catalog no. PHR1199-500MG, Sigma Aldrich), 400 mg

of calcium carbonate (catalog no. 239216-500g, Sigma Aldrich), 650 mg of glucose (catalog no. G8270-100G, Sigma Aldrich), 800 mg of potassium chloride (catalog no. 60128-250G-F, Sigma Aldrich), 1 gm of BSA (catalog no. A7906-50G, Sigma Aldrich), 2.5 gm of pepsin (catalog no. P7000-25G, Sigma Aldrich), and 3 gm of mucin (catalog no. M2378-100G, Sigma Aldrich) where suspended into 500 mL of deionized water and mixed on a stir plate at 500 RPM for 5 minutes. After dissolving all materials, add roughly 1 mL of 12M hydrogen chloride (catalog no. H1758-100Ml, Sigma Aldrich) solution to make the pH to 1. In a 50 mL polypropylene tube, we added 25 mL of the 'Gastric Juice Mastermix' and 1 mg per mL of the PAH-loaded Nanoparticles. We placed these tubes on a shaker and harvested at intervals, 30 minutes, 1.5 hours, and 3.5 hours in order to simulate the potential exposure time to the stomach post ingestion. Post-harvest, we spun down a tube at 5000 G for 10 minutes and removed the supernatant, which contained the 'Gastric Juice Mastermix'. The nanoparticle pellet that remained was resuspended and added 1 mL of 2M sodium hydroxide solution (catalog no. S5881-500G, Sigma Aldrich) to dissolve the pallet. Next, add 15 mL of DCM and placed on the shaker for 48 hours. The DCM layer was transferred to glass scintillation vials that were dried under vacuum. The remaining PAHs and particles were resuspended into 250 µL of DCM and loaded into glass vials to be run on GC-MS. The GC-MS protocol for PAH analysis was from a published paper by the vendor. Samples were fit to a standard curve and the concentration was calculated.

Analysis of PAH loaded nanoplastics in small intestine conditions were performed in the same manner as above. However, the composition of the 'Duodenum Juices' differed, composed of 565 mg of potassium chloride, 7 gm of sodium chloride (catalog no. S7653-250G, Sigma Aldrich), 5800 mg of sodium bicarbonate (catalog no. S5761-1KG, Sigma Aldrich), 50 mg of magnesium chloride (catalog no. M8266-100G, Sigma Aldrich), 80 mg of potassium phosphate monobasic (catalog no. P5655-1KG, Sigma Aldrich), 100 mg of urea (catalog no. U5378-1KG, Sigma Aldrich), 200 mg of calcium chloride (catalog no. C3881-500G, Sigma Aldrich), 1 gm of BSA (catalog no. A7906-50G, Sigma Aldrich), 9 gm of pancreatin (catalog no. P7545-25G, Sigma Aldrich), and 1.5 gm of lipase (catalog no. L3126-100G, Sigma Aldrich) where suspended into 500 mL of deionized water and mixed on a stir plate at 500 RPM for 5 minutes. After dissolving all materials, add roughly 1.5 mL of 12M hydrogen chloride solution.

In another clean beaker, add 400 mg of potassium chloride, 5.25 gm of sodium chloride 5.8 gm of sodium bicarbonate, 250 mg of urea, 250 mg of calcium chloride, 1.8 gm of BSA, and 30 g of bile (catalog no. B8381-100G, Sigma Aldrich) and fill with 500 mL of deionized water to create 'Bile Juices'. After 5 minutes stirring, add roughly 1.25 mL of 12M hydrogen chloride solution.

To simulate small intestine environments, we added 25 mL of the 'Duodenum Juices' and 1 mg per mL of the PAH-loaded Nanoparticles in to a 50-mL polypropylene tube. We placed these tubes on a shaker and harvested for 30 minutes. Post-harvest, we spun down a tube at 5000 G for 10 minutes and removed the supernatant, which contained the 'Duodenum Juices'. We added 25 mL of 'Bile Juices' on it and spined for 30 seconds to dissolve nanoparticles pallet, which from previous step, with 'Bile Juices' well. After mixing, we placed these tubes on a shaker and harvested at intervals, 30 minutes, 3.5 hours, and 7.5 hours in order to simulate the potential exposure time to the small intestine post ingestion. Post-harvest, we spun down a tube at 5000 G for 10 minutes and removed the supernatant, which contained the 'Bile Juices'. The nanoparticle pellet that remained was resuspended and added 1 mL of sodium hydroxide solution (catalog no. S5881-500G, Sigma Aldrich) to dissolve the pallet. Next, we added 15 mL of DCM and placed on the shaker for 48 hours. Next, the DCM layer was transferred to glass scintillation vials that were dried under vacuum. The remaining PAHs and particles were resuspended into 250 microliters of DCM and loaded into glass vials to be run on GC-MS. The GC-MS protocol for PAH analysis was from a published paper by the vendor. Samples were fit to a standard curve and the concentration was calculated.

Statistical Information

Kruskal-Wallis test was performed for zeta potential measurements. Mann-Whitney tests were performed to compare day 2 vs. day 3 sorption for native, week 5, and week 10. Tukey's multiple comparison was used for comparing 24, 48, and 72 hour PAH sorption times points. Brown-Forsy, Welch's Anova test, and Wilcoxon matched-pairs signed rank test were performed for sorption experiments displayed in **Supporting Information Table**3. 2way ANOVA test was performed PAH gastro and intestinal desorption plots for native,

week 5, and week 10. Kruskal-Wallist tests and Wilcoxon matched-pairs signed rank tests were performed for desorption experiments displayed in Supporting Information Table 3. **: p < 0.01, *: p < 0.05, ns: p > 0.05.

717 AUTHOR INFORMATION

- 718 Correspondence Author Björn M. Reinhard,
- 719 Department of Chemistry and Division of Materials Science and Engineering,
- 720 Boston University, The Photonics Center 706B, 8 St. Mary's Street, Boston, MA, 02214
- 721 Email bmr@bu.edu · Phone 617-353-8669 · Fax 617-353-6466
- 722 **Author Contributions** B.M.R. conceived the study. E.B.S. and B.M.R. designed the
- experiments. E.B.S. and W.G. performed all experiments. E.B.S. analyzed the data. E.B.S.
- and B.M.R. interpreted the data. E.B.S. and B.M.R. wrote the manuscript.
- 725 Funding Sources B.M.R. acknowledges support from the National Science Foundation
- through grant CBET-2032376.
- 727 **Competing Interests** The authors declare no competing interests.
- 728 Code availability All data and code available upon request.
- 729 Acknowledgements We thank Plastics Sustainable Coastlines Hawaii, facilitated by
- Rebecca Mattos, for the shipping of plastics and to all representatives from Sustainable
- 731 Coastlines Hawaii, Sea Cleaners New Zealand, and Nā Kama Kaiha at Kahuku Beach on
- O'ahu that helped collect the plastics. We thank Meghan K. Bruckman for help developing
- 733 the table of content artwork. XPS measurements were performed at the Center for
- Nanoscale Systems (CNS), a member of the National Nanotechnology Coordinated
- Infrastructure Network (NNCI). It is supported by the National Science Foundation under
- 736 NSF award no. 1541959. CNS is part of Harvard University.

737

738

739

740

741

742

743

744

745

746

ASSOCIATED CONTENT

SUPPORTING INFORMATION

Supplemental information and methods regarding investigation of hydrophobicity and surface morphology using Rose Bengal assays and STED microscopy, scheme of weathering protocol, spectrum of light applied during weathering, XPS and DSC characterization of nanoplastics, additional FTIR spectra of nanoplastics and of plastics collected in nature, SEM images of nanoplastics, FTIR database look ups, scheme of PET degradation products, list of calcium carbonate vibrational modes, MP-AES data, GC-MS data of filtrate, PAH loading and desorption measurements and statistics, principle component contributions and SVM model confusion matrix accuracy testing, FTIR band assignments and references, gastric and intestinal juice compositions, PAH bioaccessibility statistics.

_

REFERENCES

784

- 785 1. Plastics the Facts 2021, https://plasticseurope.org/knowledge-
- hub/plastics-the-facts-2021/, accessed 02/27/2023.
- 787 2. Frias, J. P. G. L.; Nash, R. Microplastics: Finding a Consensus on the Definition.
- 788 *Mar. Pollut. Bull.* **2019,** *138,* 145-147.
- 789 3. Kaabel, S.; Therien, J. P. D.; Deschênes, C. E.; Duncan, D.; Friščić, T.; Auclair,
- 790 K. Enzymatic Depolymerization of Highly Crystalline Polyethylene Terephthalate
- 791 Enabled in Moist-Solid Reaction Mixtures. *Proc Natl Acad Sci U S A* **2021,** *118* (29).
- 4. Agency, E. P. Plastics: Material-Specific Data. EPA, E. P. A., Ed. 30 Sept. 2021.
- 793 5. Geyer, R.; Jambeck, J. R.; Law, K. L. Production, Use, and Fate of All Plastics
- 794 Ever Made. *Sci Adv* **2017**, *3* (7), e1700782.
- 795 6. OECD. Global Plastics Outlook: Policy Scenarios to 2060; OECD Publishing,
- 796 2022. DOI:10.1787/aa1edf33-en
- 797 7. Pivorkonsky, M.; Cermakova, L.; Novotna, K.; Peer, P.; Cajthaml, T.; Janda, V.
- 798 Occurrence of Microplastics in Raw and Treated Drinkinh Water. *Sci. Total Environ.*
- 799 **2018,** *643*, 1644-1651.
- 800 8. Jambeck, J. R.; Geyer, R.; Wilcox, C.; Siegler, T. R.; Perryman, M.; Andrady,
- 801 A.; Narayan, R.; Law, K. L. Marine Pollution. Plastic Waste Inputs from Land into the
- 802 Ocean. Science **2015**, 347 (6223), 768-71.
- 803 9. Rhodes, C. J. Plastic Pollution and Potential Solutions. *Sci Prog* **2018**, *101* (3),
- 804 207-260.
- 805 10. Alimi, O. S.; Farner Budarz, J.; Hernandez, L. M.; Tufenkji, N. Microplastics
- and Nanoplastics in Aquatic Environments: Aggregation, Deposition, and Enhanced
- 807 Contaminant Transport. Environmental Science & Technology 2018, 52 (4), 1704-
- 808 1724.
- 809 11. Cózar, A.; Echevarría, F.; González-Gordillo, J. I.; Irigoien, X.; Ubeda, B.;
- 810 Hernández-León, S.; Palma, A. T.; Navarro, S.; García-de-Lomas, J.; Ruiz, A.;
- 811 Fernández-de-Puelles, M. L.; Duarte, C. M. Plastic Debris in the Open Ocean. *Proc Natl*
- 812 *Acad Sci U S A* **2014,** *111* (28), 10239-44.
- 813 12. Thompson, R. C.; Olson, Y.; Mitchell, R. P.; Davis, A.; Rowland, S. J.; John, A.
- W.; McGonigle, D.; Russel, A. E. Lost at Sea: Where Is All the Plastic? Science 2004,
- 815 *304*, 838.
- 816 13. Jiang, B.; Kauffman, A. E.; Li, L.; McFee, W.; Cai, B.; Weinstein, J.; Lead, J. R.;
- Chatterjee, S.; Scott, G. I.; Xiao, S. Health Impacts of Environmental Contamination of
- 818 Micro- and Nanoplastics: A Review. Environ Health Prev Med 2020, 25 (1), 29.
- 819 14. Yaripour, S.; Huuskonen, H.; Rahman, T.; Kekäläinen, J.; Akkanen, J.; Magris,
- 820 M.; Kipriianov, P. V.; Kortet, R. Pre-Fertilization Exposure of Sperm to Nano-Sized
- Plastic Particles Decreases Offspring Size and Swimming Performance in the
- 822 European Whitefish (Coregonus Lavaretus). Environmental Pollution 2021, 291,
- 823 118196.
- 824 15. Gupta, C.; Kaushik, S.; Himanshu; Jain, S.; Dhanwani, I.; Mansi; Garg, S.;
- Paul, A.; Pant, P.; Gupta, N. Bioaccumulation and Toxicity of Polystyrene
- Nanoplastics on Marine and Terrestrial Organisms with Possible Remediation
- 827 Strategies: A Review. *Environmental Advances* **2022**, *8*, 100227.

- 828 16. Bouwmeester, H.; Hollman, P. C.; Peters, R. J. Potential Health Impact of
- 829 Environmentally Released Micro- and Nanoplastics in the Human Food Production
- 830 Chain: Experiences from Nanotoxicology. Environ Sci Technol 2015, 49 (15), 8932-
- 831 47.
- 832 17. Teng, M.; Zhao, X.; Wang, C.; Wang, C.; White, J. C.; Zhao, W.; Zhou, L.;
- Duan, M.; Wu, F. Polystyrene Nanoplastics Toxicity to Zebrafish: Dysregulation of
- the Brain–Intestine–Microbiota Axis. *ACS Nano* **2022**, *16* (5), 8190-8204.
- 835 18. Xu, E. G.; Cheong, R. S.; Liu, L.; Hernandez, L. M.; Azimzada, A.; Bayen, S.;
- 836 Tufenkji, N. Primary and Secondary Plastic Particles Exhibit Limited Acute Toxicity
- but Chronic Effects on Daphnia Magna. Environmental Science & Technology 2020,
- 838 *54* (11), 6859-6868.
- 839 19. Deng, Y.; Zhang, Y.; Lemos, B.; Ren, H. Tissue Accumulation of Microplastics
- in Mice and Biomarker Responses Suggest Widespread Health Risks of Exposure. Sci
- 841 *Rep* **2017,** *7*, 46687.
- 842 20. Yang, Y. F.; Chen, C. Y.; Lu, T. H.; Liao, C. M. Toxicity-Based
- 843 Toxicokinetic/Toxicodynamic Assessment for Bioaccumulation of Polystyrene
- 844 Microplastics in Mice. *J Hazard Mater* **2019**, *366*, 703-713.
- 845 21. Zhang, C.; Chen, J.; Ma, S.; Sun, Z.; Wang, Z. Microplastics May Be a
- 846 Significant Cause of Male Infertility. *American Journal of Men's Health* **2022,** 16 (3),
- 847 15579883221096549.
- 848 22. Schwabl, P.; Köppel, S.; Königshofer, P.; Bucsics, T.; Trauner, M.; Reiberger,
- 849 T.; Liebmann, B. Detection of Various Microplastics in Human Stool: A Prospective
- 850 Case Series. *Ann Intern Med* **2019**, *171* (7), 453-457.
- 851 23. Bakir, A.; Rowland, S. I.; Thompson, R. C. Enhanced Desorption of Persistent
- Organic Pollutants from Microplastics under Simulated Physiological Conditions.
- 853 *Environmental Pollution* **2014**, *185*, 16-23.
- 854 24. Browne, Mark A.; Niven, Stewart J.; Galloway, Tamara S.; Rowland, Steve J.;
- Thompson, Richard C. Microplastic Moves Pollutants and Additives to Worms,
- Reducing Functions Linked to Health and Biodiversity. *Current Biology* **2013**, *23*
- 857 (23), 2388-2392.
- 858 25. Hartmann, N. B.; Rist, S.; Bodin, J.; Jensen, L. H.; Schmidt, S. N.; Mayer, P.;
- Meibom, A.; Baun, A. Microplastics as Vectors for Environmental Contaminants:
- 860 Exploring Sorption, Desorption, and Transfer to Biota. *Integr Environ Assess Manag*
- 861 **2017,** *13* (3), 488-493.
- 862 26. Koelmans, A. A.; Bakir, A.; Burton, G. A.; Janssen, C. R. Microplastic as a
- Vector for Chemicals in the Aquatic Environment: Critical Review and Model-
- 864 Supported Reinterpretation of Empirical Studies. *Environ Sci Technol* **2016**, *50* (7),
- 865 3315-26.
- 866 27. Ogata, Y.; Takada, H.; Mizukawa, K.; Hirai, H.; Iwasa, S.; Endo, S.; Mato, Y.;
- 867 Saha, M.; Okuda, K.; Nakashima, A.; Murakami, M.; Zurcher, N.; Booyatumanondo,
- 868 R.; Zakaria, M. P.; Dung le, Q.; Gordon, M.; Miguez, C.; Suzuki, S.; Moore, C.;
- 869 Karapanagioti, H. K.; Weerts, S.; McClurg, T.; Burres, E.; Smith, W.; Van
- Velkenburg, M.; Lang, J. S.; Lang, R. C.; Laursen, D.; Danner, B.; Stewardson, N.;
- 871 Thompson, R. C. International Pellet Watch: Global Monitoring of Persistent Organic
- Pollutants (Pops) in Coastal Waters. 1. Initial Phase Data on Pcbs, Ddts, and Hchs.
- 873 *Mar Pollut Bull* **2009,** *58* (10), 1437-46.

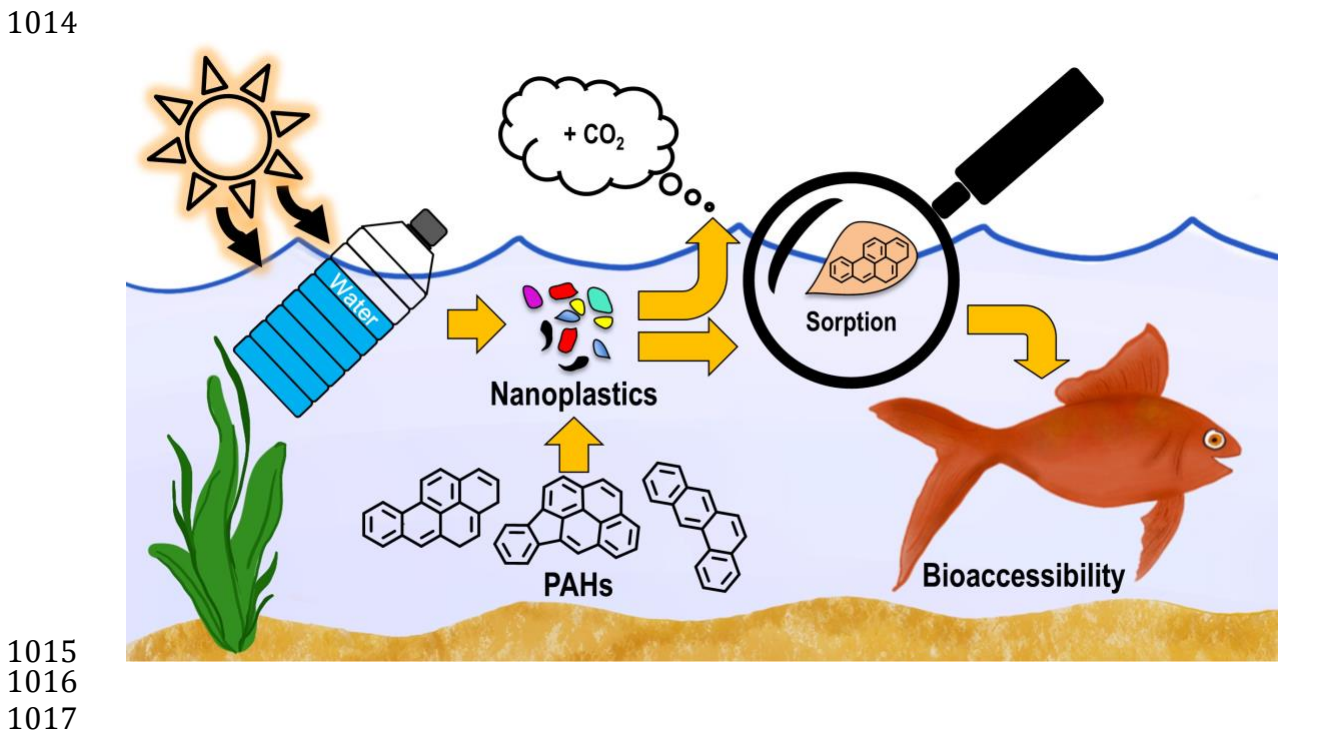
- 874 28. Blanton, R. H.; Lyte, M.; Myers, M. J.; Bick, P. H. Immunomodulation by
- Polyaromatic Hydrocarbons in Mice and Murine Cells. Cancer Res 1986, 46 (6),
- 876 2735-9.
- 29. Dasgupta, P. S.; Lahiri, T. Alteration of Brain Catecholamines During Growth
- of Benzo(a)Pyrene Induced Murine Fibrosarcoma. *Neoplasma* **1992**, *39* (3), 163-5.
- 879 30. Szczeklik, A.; Szczeklik, J.; Galuszka, Z.; Musial, J.; Kolarzyk, E.; Targosz, D.
- Humoral Immunosuppression in Men Exposed to Polycyclic Aromatic Hydrocarbons
- and Related Carcinogens in Polluted Environments. Environ Health Perspect 1994,
- 882 *102* (3), 302-4.
- 883 31. Harris, K. L.; Banks, L. D.; Mantey, J. A.; Huderson, A. C.; Ramesh, A.
- 884 Bioaccessibility of Polycyclic Aromatic Hydrocarbons: Relevance to Toxicity and
- Carcinogenesis. *Expert Opin Drug Metab Toxicol* **2013**, 9 (11), 1465-80.
- 886 32. Avio, C. G.; Gorbi, S.; Milan, M.; Benedetti, M.; Fattorini, D.; d'Errico, G.;
- Pauletto, M.; Bargelloni, L.; Regoli, F. Pollutants Bioavailability and Toxicological
- Risk from Microplastics to Marine Mussels. *Environ Pollut* **2015**, *198*, 211-22.
- 889 33. Harris, K. L.; Banks, L. D.; Mantey, J. A.; Huderson, A. C.; Ramesh, A.
- 890 Bioaccessibility of Polycyclic Aromatic Hydrocarbons: Relevvance to Toxicity and
- 891 Carcinogenesis. Expert. Opin. Drug Metab. Toxicol. 2013, 9, 1465-1480.
- 892 34. Magrì, D.; Sánchez-Moreno, P.; Caputo, G.; Gatto, F.; Veronesi, M.; Bardi, G.;
- 893 Catelani, T.; Guarnieri, D.; Athanassiou, A.; Pompa, P. P.; Fragouli, D. Laser Ablation
- as a Versatile Tool to Mimic Polyethylene Terephthalate Nanoplastic Pollutants:
- Characterization and Toxicology Assessment. ACS Nano 2018, 12 (8), 7690-7700.
- 896 35. Chamas, A.; Moon, H.; Zheng, J.; Qiu, Y.; Tabassum, T.; Jang, J. H.; Abu-Omar,
- 897 M.; Scott, S. L.; Suh, S. Degradation Rates of Plastics in the Environment. *ACS*
- 898 *Sustainable Chemistry & Engineering* **2020**, *8* (9), 3494-3511.
- 899 36. Mattsson, K.; Hansson, L. A.; Cedervall, T. Nano-Plastics in the Aquatic
- 900 Environment. *Environ Sci Process Impacts* **2015**, *17* (10), 1712-21.
- 901 37. Andrade, J.; Fernández-González, V.; López-Mahía, P.; Muniategui, S. A Low-
- 902 Cost System to Simulate Environmental Microplastic Weathering. *Marine Pollution*
- 903 *Bulletin* **2019**, *149*, 110663.
- 904 38. Kester, D. R.; Duedall, I. W.; Connors, D. N.; Pytkowicz, R. M. Preparation of
- 905 Artificial Seawater. *Limnology and Oceanography* **1967,** *12* (1), 176-179.
- 906 39. El Hadri, H.; Gigault, I.; Maxit, B.; Grassl, B.; Reynaud, S. Nanoplastic from
- 907 Mechanically Degraded Primary and Secondary Microplastics for Environmental
- 908 Assessments. *NanoImpact* **2020,** *17*, 100206.
- 909 40. Pudack, C.; Stepanski, M.; Fässler, P. Pet Recycling Contributions of
- 910 Crystallization to Sustainability. *Chemie Ingenieur Technik* **2020,** 92 (4), 452-458.
- 911 41. Liang, C. Y.; Krimm, S. Infrared Spectra of High Polymers: Part Ix.
- Polyethylene Terephthalate. *Journal of Molecular Spectroscopy* **1959**, *3* (1), 554-574.
- 913 42. Andersen, F. A.: Brečević, L. Infrared Spectra of Amorphous and Crystalline
- 914 Calcium Carbonate. *Acta Chem. Scand.*, **1991**, 45, *1018-1024*.
- 915 43. Edge, M.; Wiles, R.; Allen, N. S.; McDonald, W. A.; Mortlock, S. V.
- 916 Characterisation of the Species Responsible for Yellowing in Melt Degraded
- 917 Aromatic Polyesters—I: Yellowing of Poly(Ethylene Terephthalate). *Polymer*
- 918 *Degradation and Stability* **1996,** *53*, 141-151.

- 919 44. Donelli, I.; Freddi, G.; Nierstrasz, V. A.; Taddei, P. Surface Structure and
- 920 Properties of Poly-(Ethylene Terephthalate) Hydrolyzed by Alkali and Cutinase.
- 921 *Polymer Degradation and Stability* **2010,** 95 (9), 1542-1550.
- 922 45. Alzuhairi, M.; Khalil, B.; Hadi, R. S. Nano Zno Catalyst for Chemical Recycling
- 923 of Polyethylene Terephthalate (Pet). Engineering Technology Journal
- 924 **2017,** *35*, 831-837.
- 925 46. Sang, T.; Wallis, C. J.; Hill, G.; Britovsek, G. J. P. Polyethylene Terephthalate
- 926 Degradation under Natural and Accelerated Weathering Conditions. *European*
- 927 *Polymer Journal* **2020**, *136*, 109873.
- 928 47. Xu, B.; Poduska, K. M. Linking Crystal Structure with Temperature-Sensitive
- 929 Vibrational Modes in Calcium Carbonate Minerals. Physical Chemistry Chemical
- 930 *Physics* **2014**, *16* (33), 17634-17639.
- 931 48. Aylward, G. F., Tristan. SI Chemical Data Book (4th ed.). John Wiley & Sons
- 932 Australia: 2008.
- 933 49. Rohleder, J. K., E. . Calcium Carbonate: From the Cretaceous Period Into the
- 934 *21st Century.* Springer Science & Business Media.: 2001.
- 935 50. Ballesteros-Soberanas, J.; Hernández-Garrido, J. C.; Cerón-Carrasco, J. P.;
- 936 Leyva-Pérez, A. Selective Semi-Hydrogenation of Internal Alkynes Catalyzed by Pd-
- 937 Caco3 Clusters. *Journal of Catalysis* **2022**, *408*, 43-55.
- 938 51. Al Omari, M. M.; Rashid, I. S.; Qinna, N. A.; Jaber, A. M.; Badwan, A. A. Calcium
- 939 Carbonate. *Profiles Drug Subst Excip Relat Methodol* **2016**, *41*, 31-132.
- 940 52. Ioakeimidis, C.; Fotopoulou, K. N.; Karapanagioti, H. K.; Geraga, M.; Zeri, C.;
- Papathanassiou, E.; Galgani, F.; Papatheodorou, G. The Degradation Potential of Pet
- Bottles in the Marine Environment: An Atr-Ftir Based Approach. *Scientific Reports*
- 943 **2016**, *6* (1), 23501.
- 944 53. Beltrán-Sanahuja, A.; Casado-Coy, N.; Simó-Cabrera, L.; Sanz-Lazaro, C.
- 945 Monitoring Polymer Degradation under Different Conditions in the Marine
- 946 Environment. *Environmental Pollution* **2019**, *259*, 113836.
- 947 54. Shams, M.; Alam, I.; Chowdhury, I. Interactions of Nanoscale Plastics with
- 948 Natural Organic Matter and Silica Surfaces Using a Quartz Crystal Microbalance.
- 949 Water Research **2021**, 197, 117066.
- 950 55. Velzeboer, I.; Kwadijk, C. J. A. F.; Koelmans, A. A. Strong Sorption of Pcbs to
- Nanoplastics, Microplastics, Carbon Nanotubes, and Fullerenes. *Environmental*
- 952 *Science & Technology* **2014**, *48* (9), 4869-4876.
- 953 56. Ribière, C.; Peyret, P.; Parisot, N.; Darcha, C.; Déchelotte, P. J.; Barnich, N.;
- Peyretaillade, E.; Boucher, D. Oral Exposure to Environmental Pollutant
- 955 Benzo[a]Pyrene Impacts the Intestinal Epithelium and Induces Gut Microbial Shifts
- 956 in Murine Model. *Sci Rep* **2016**, *6*, 31027.
- 957 57. IARC. Some Non-Heterocyclic Polycyclic Aromatic Hydrocarbons and Some
- 958 Related Exposures. *IARC Monogr Eval Carcinog Risks Hum* **2010**, 92, 1-853.
- 959 58. Versantvoort, C. H. M.; Oomen, A. G.; Van de Kamp, E.; Rompelberg, C. J. M.;
- 960 Sips, A. J. A. M. Applicability of an in Vitro Digestion Model in Assessing the
- 961 Bioaccessibility of Mycotoxins from Food. Food and Chemical Toxicology 2005, 43
- 962 (1), 31-40.
- 963 59. Goodman, B. E. Insights into Digestion and Absorption of Major Nutrients in
- 964 Humans. *Advances in physiology education* **2010**, *34* (2), 44-53.

- 965 60. Mudie, D. M.; Murray, K.; Hoad, C. L.; Pritchard, S. E.; Garnett, M. C.;
- 966 Amidon, G. L.; Gowland, P. A.; Spiller, R. C.; Amidon, G. E.; Marciani, L.
- 967 Quantification of Gastrointestinal Liquid Volumes and Distribution Following a 240
- 968 Ml Dose of Water in the Fasted State. *Molecular Pharmaceutics* **2014,** *11* (9), 3039-
- 969 3047.
- 970 61. Schiller, C.; Fröhlich, C. P.; Giessmann, T.; Siegmund, W.; Mönnikes, H.;
- 971 Hosten, N.; Weitschies, W. Intestinal Fluid Volumes and Transit of Dosage Forms as
- 972 Assessed by Magnetic Resonance Imaging. *Aliment Pharmacol Ther* **2005,** *22* (10),
- 973 971-9.

- 974 62. Smith, K. E.; Oostingh, G. J.; Mayer, P. Passive Dosing for Producing Defined
- 975 and Constant Exposure of Hydrophobic Organic Compounds During in Vitro Toxicity
- 976 Tests. *Chem Res Toxicol* **2010**, *23* (1), 55-65.

Table of Content Artwork



Legend

Macroscopic plastics in the environment experience persistent UV-induced and mechanical stress, resulting in the formation of nanoplastics that can mobilize carcinogens into the environment and the food chain.

Nanoplastics Weathering and Polycyclic

1044 Aromatic Hydrocarbon Mobilization

1045	Erik B. Schiferle ^{3,2,1} , Wenxu $Ge^{1,2}$, and Björn M. Reinhard ^{1,2,3*}
1046	
1047	¹ Department of Chemistry, ² The Photonics Center, ³ Division of Materials Science and
1048	Engineering, Boston University, Boston, MA, 02215, USA.
1049	*E-mail: bmr@bu.edu
1050	
1051	
1052	
1053	Supporting Information
1054	
1055	
1056	
1057	
1058	
1059	
1060	
1061	
1062	
1063	
1064	
1065	
1066	
1067	
1068	

Sorption validation and visualization

The photochemical weathering of nanoplastics is associated with changes in the surface morphology and structure as well as the chemical composition and surface charge of nanoplastics. These factors affect the capacity of nanoplastics to sorb hydrophobic molecules as seen with respect to PAH sorption in Figure 4A. To validate the trends observed for PAHs. Rose Bengal assays were performed (Figure S7A).¹⁻³ In agreement with the findings for PAHs, photochemical weathering decreased the affinity for sorption of the hydrophobic Rose Bengal, confirming a loss in hydrophobicity. A similar qualitative result was obtained by quantifying the amount of unbound hydrophilic (STAR Orange) and hydrophobic (STAR 635) dye after incubation with nanoplastics (Figure S7B), which revealed more hydrophilic dye associated with the nanoplastics after weathering. Intriguingly, imaging studies of the hydrophilic, hydrophobic dyes revealed that they are not homogenously distributed across the plastic surface (Figure S7C). Instead, regions with more hydrophobic or hydrophilic character are discernible, which may have implications for the concept of bioaccessiblity on fundamental NP – cell interactions. Importantly, analysis of red vs. green pixel intensity and prevalence illustrated the same ratio of hydrophobicity to hydrophilicity as observed in the bulk.

1101 SUPPORTING INFORMATION METHODS 1102 1103 Rose Bengal 1104 Rose Bengal sodium salt (RB) was obtained from Sigma–Aldrich (catalog no. 330000-1G). 1105 RB was suspended in ultrapure water from MiliQ at a concentration of 100 [ug/mL]. 1106 Nanoplastics of varying concentrations were suspended in 200 µL of ultrapure water. 50 1107 uL of RB stock solution was added to the nanoplastics solution, resulting in a concentration of 20 ug/mL of Rose Bengal. Samples were incubated overnight on a shaker in the dark. 1108 1109 Samples were spun down at 20,000 G for 10 minutes. 200 µL of supernatant was moved 1110 to a new Eppendorf tube. Absorbance values of 100 µL of this stock were collected on a 1111 Cary 5000 UV-Vis-NIR between 400 and 650 nm. Absorbance intensity at 549 nm was fit 1112 to a standard curve generated by series dilution of stock Rose Bengal. Rose Bengal bound 1113 to particle was calculated by subtracting free Rose Bengal concentration from starting Rose Bengal concentration of 20 µg/mL as previously reported.^{1, 2} 1114 1115 1116 STED Microscopy 1117 STED-specific dyes where procured from Abberior Instruments America LLC (Bethesda, 1118 MD). Upon suggestion from the vendor, we procured Abberior STAR 635, carboxylic acid (Abberior, catalog no. ST635-0001-1MG) and STAR Orange dye (Abberior, catalog no. 1119 1120 STORANGE-0001-1MG), which were the most hydrophobic and hydrophilic dyes sold, 1121 respectively. Determination of the hydrophobicity ratio was determined using a Carry 5000 1122 UV-VIS-NIR. Baseline correction was performed using OriginLab Software (Origin, 1123 Northampton, Massachusetts). The hydrophobicity ratio was determined by taking the ratio 1124 of the absorbance maxima for the two dyes. Microscope images were performed on the 1125 Abberior STED super-resolution microscope using the 2D option as significant particle 1126 movement was observed for long exposure times required for 3D image construction due 1127 to the high powered lasers. 1128 1129 1130 1131 1132

1133 SUPPORTING FIGURES

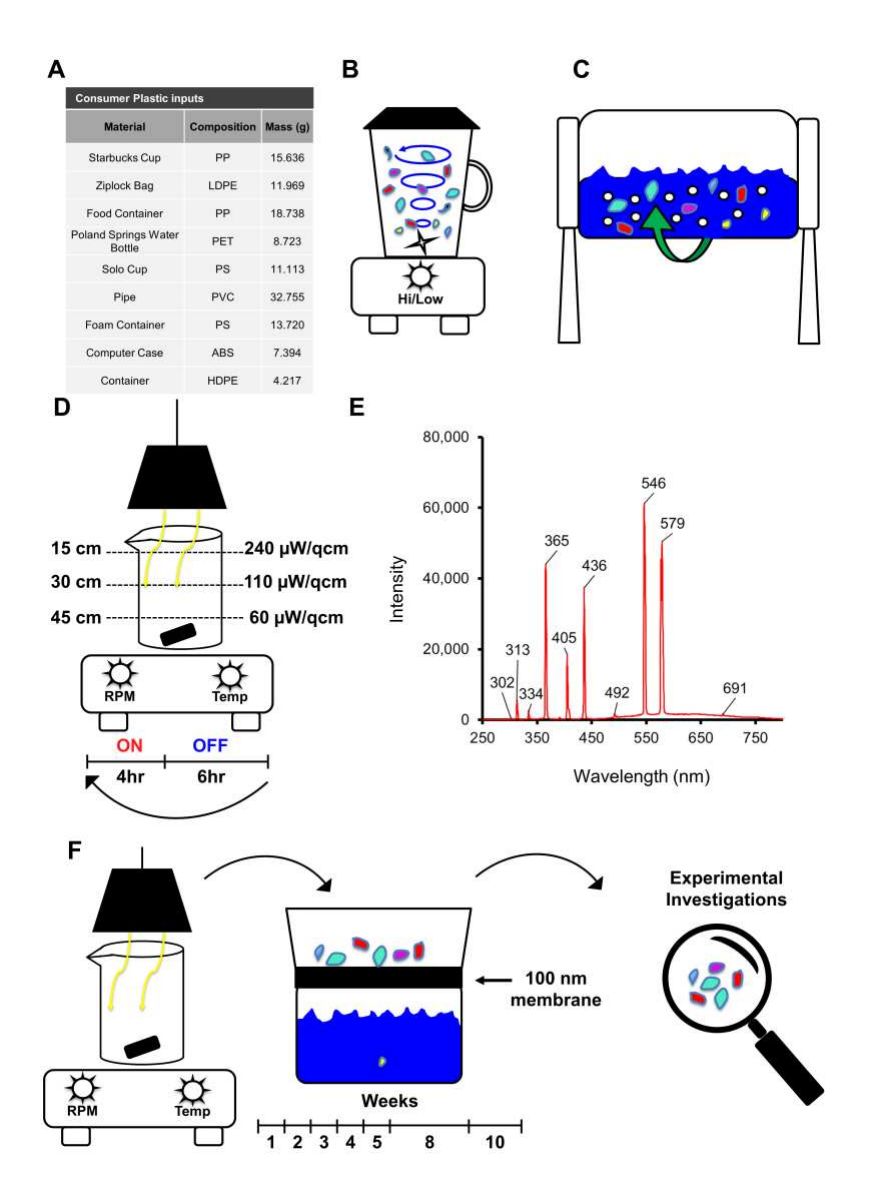


Figure S1. Weathering Protocol and Schematic

- (A) Table of starting materials used to make nanoplastics, illustrating composition according to vendor and the mass (gram, g) utilized in the milling process.
- 1138 **(B)** Diagram of the blending process used to make small pieces for the ball mill. 1139
 - (C) Schematic of the ball mill.

1134 1135

1136

1137

1146

- 1140 (D) Weathering device displaying kinetics as well as power of UV-A + UV-B, provided by the vendor, as a function of distance from the light source (power vs. distance from lamp 1141 1142 relative to beaker not to scale).
- 1143 (E) Spectra of light used for the accelerated weathering process. Intensity in UVB range (280-315 nm) is attenuated in the recorded spectrum due to stronger absorption in the fiber 1144 1145 used to record the spectrum.
 - (F) Diagram depicting how the plastics were harvested.

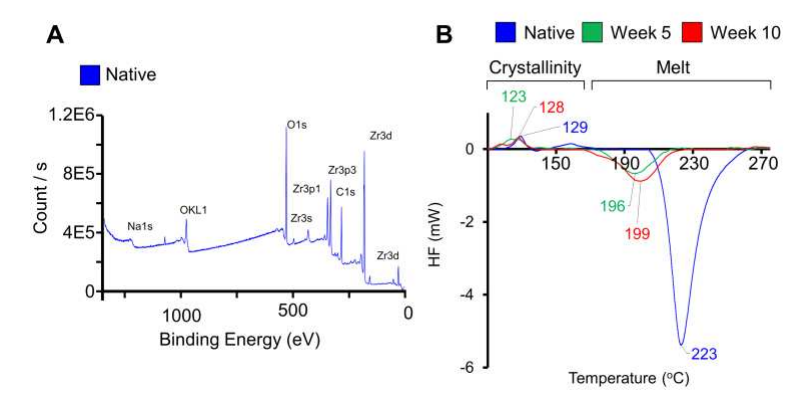


Figure S2. XPS and DSC Characterization

- (A) X-ray Photoelectron Spectroscopy (XPS) scan recording electron counts per second as a function binding energy (eV) for native nanoplastics.
- **(B)** Differential scanning calorimetry (DSC) measurements data for native, week 5, and week 10 nanoplastics.

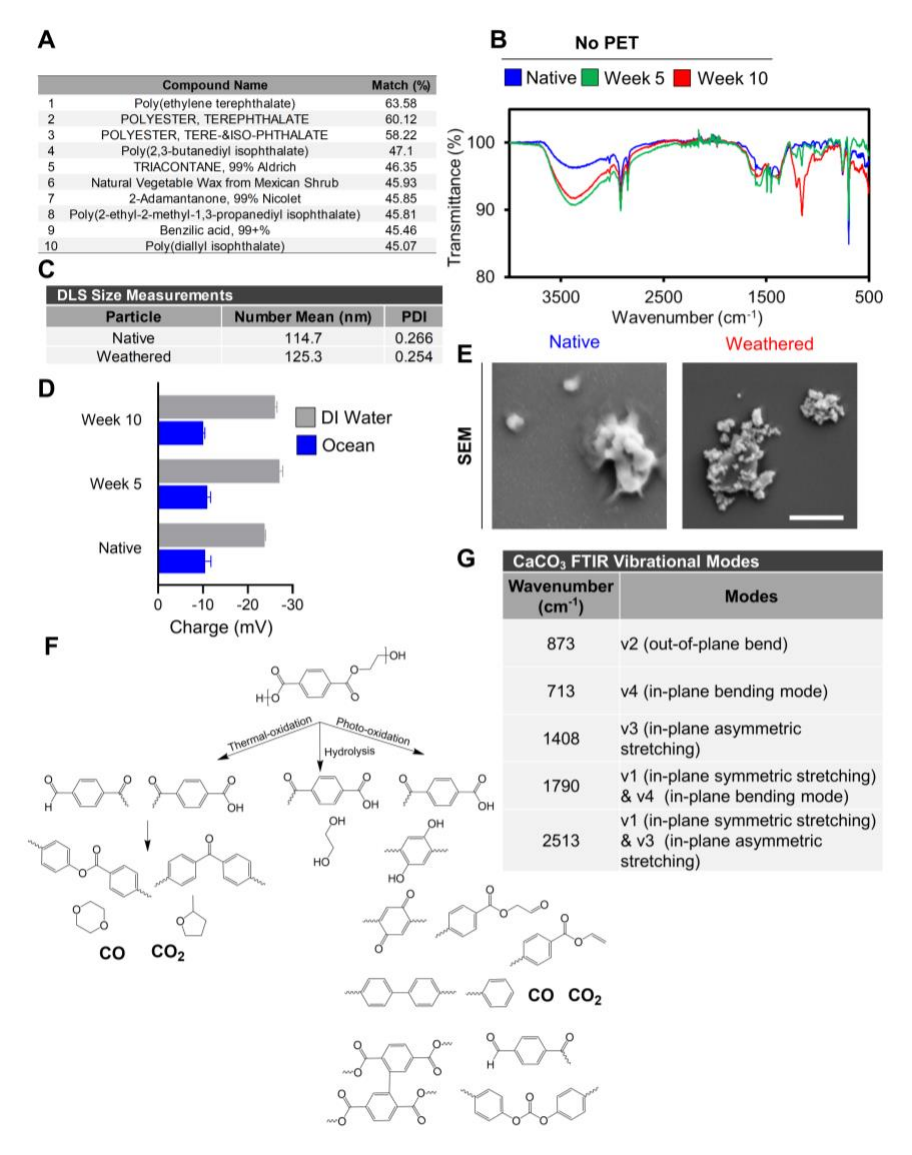


Figure S3, Plastics devoid of PET characterization, PET degradation products, and calcium carbonate vibrational modes

- **(A)** Probability match of Native nanoplastics compared to known materials from Thermo Fisher OMNIC spectrum libraries.
- **(B)** Fourier-Transform Infrared Spectroscopy (FTIR) spectra for native, post 5 weeks, and 10 weeks of weathering nanoplastics in the absence of PET as a starting constituent. Wavenumber range 500 to 4000 (cm⁻¹).
- (C) Dynamic Light Scattering (DLS) measurements for the number mean hydrodynamic diameter (nm) for native and weathered nanoplastics without PET as a starting constituent.
- **(D)** Zeta potential (meV) measurements for native, week 5, and week 10 nanoplastics without PET as a starting constituent. Error bars represent the mean \pm SD (n=3 independent weathering trials, with 3 repeated measurements).
- **(E)** Scanning electron microscope (SEM) images of nanoplastics before (native) and after weathering. Scale bar = 400 nm.
- **(F)** Known degradation products of PET plastics as a function of thermo-oxidation, hydrolysis, and photo-oxidation.
- **(G)** Known vibrational modes for CaCO₃.

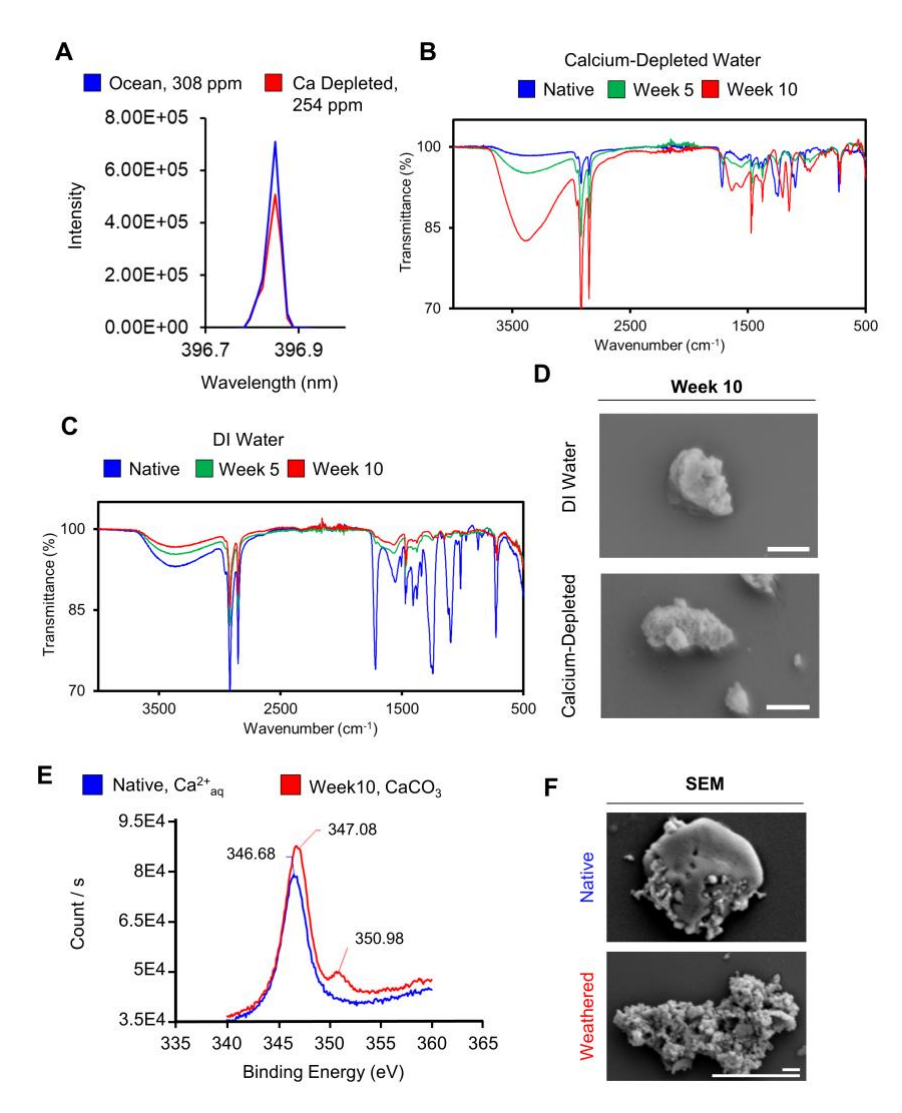


Figure S4. Calcium carbonate deposition experiments

- (A) Microwave Plasma Atomic Emission Spectroscopy (MP-AES) plot displaying intensity as a function of wavelength (nm) to compare ocean water vs. calcium-depleted ocean water. Plotted against a standard curve, calcium in parts per million (ppm) is reported.
- **(B)** Fourier-Transform Infrared Spectroscopy (FTIR) spectra for native, post 5 weeks, and 10 weeks of weathering nanoplastics in Calcium-depleted ocean water. Wavenumber range 500 to 4000 (cm-1).
- 1200 (C) Fourier-Transform Infrared Spectroscopy (FTIR) spectra for native, post 5 weeks, and 1201 10 weeks of weathering nanoplastics in deionized water. Wavenumber range 500 to 4000 (cm-1).
- **(D)** Scanning electron microscope (SEM) images of nanoplastics before (native) and after weathering. Scale bar = 400 nm.
- **(E)** XPS plot displaying electron counts per second as a function of binding energy (eV) for native and nanoplastics after photochemical weathering for 10 weeks.
- **(F)** Scanning electron microscope (SEM) images of nanoplastics before (native) and after weathering. Small Scale Bar = 200nm. Large Scale Bar = 1μm.

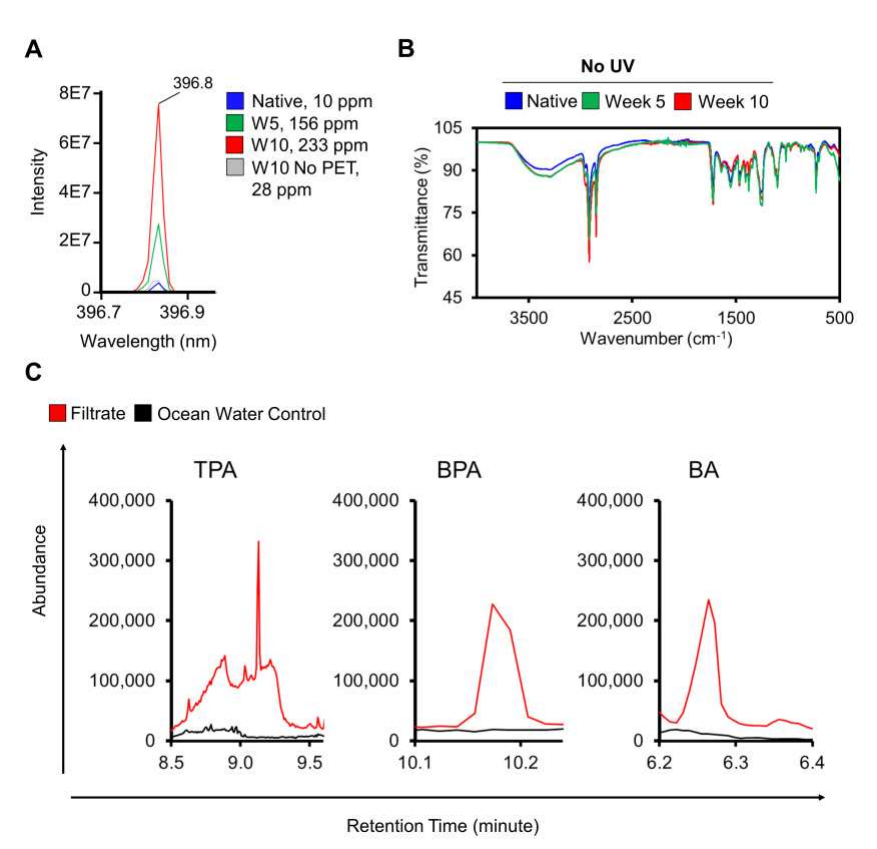


Figure S5. Calcium carbonate deposition experiments and UV degradation validation (A) Microwave Plasma Atomic Emission Spectroscopy (MP-AES) of native, week 5, and week 10 devoid of PET as a starting constituent. Plotted against a standard curve, calcium in parts per million (ppm) is reported.

(B) Fourier-Transform Infrared Spectroscopy (FTIR) spectra for native, post 5 week, and post 10 weeks of weathering nanoplastics in the dark. Ocean water was heated to the same temperatures as would be encountered with the UV light on. Wavenumber range 500 to 4000 (cm⁻¹).

(C) Gas Chromatography – Mass Spectrometry (GC-MS) plots of the filtrate collected after filtering out week 10 nanoplastics for a PET only weathering experiment. Agilent Mass Spectrometry predicts a 87% quality match to Terephthalic acid (TPA), 44% quality match to Bisphenol A (BPA), and a 91% quality match to Benzoic Acid (BA). Since the quality match was low for BPA, a commercially purchased standard was analyzed to validate the prediction for BPA.

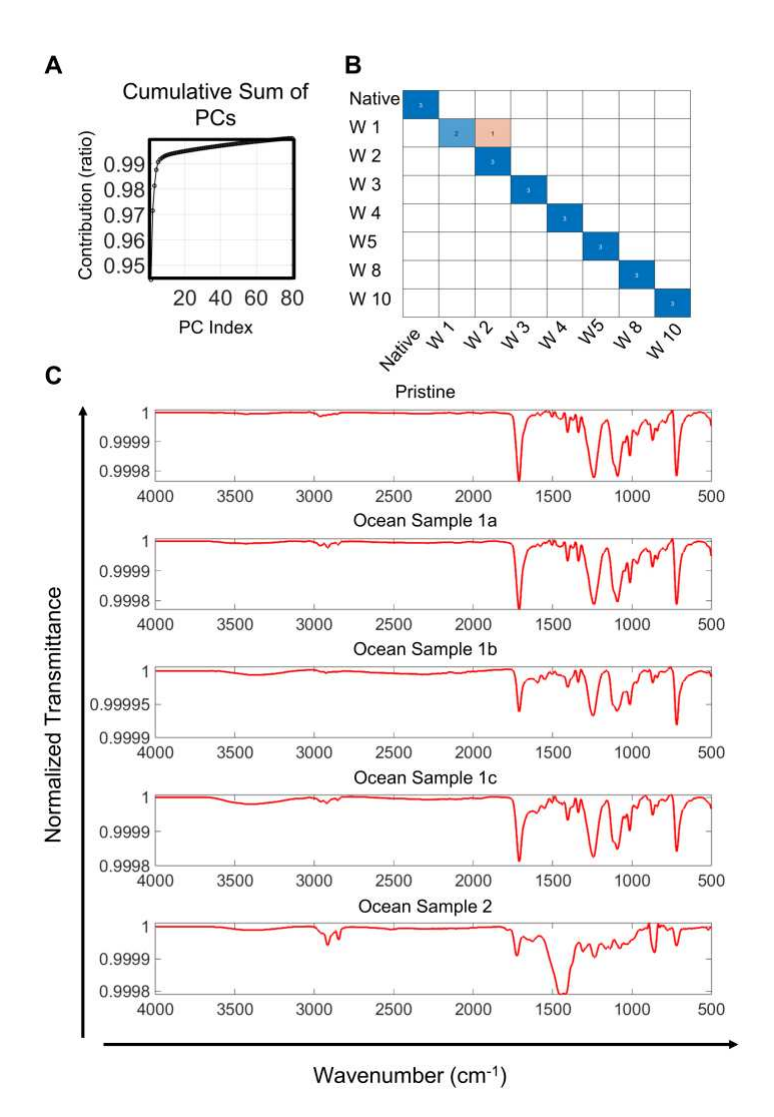
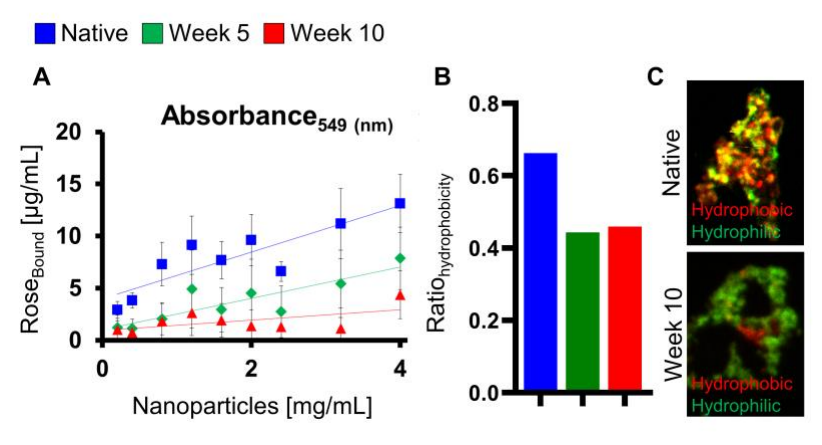


Figure S6. *Principle component analysis and support vector machine Learning studies* **(A)** Cumulative sum of principal component contribution, where all contribution sum to one and there 80 principal components in our data set.

- **(B)** SVM confusion matrix that designating the raw data on the y axis and the models prediction on the right axis. The plot demonstrates 95.833% accuracy.
- **(C)** FTIR for macroscopic plastics harvested from the ocean. Wavenumber range 500 to 4000 (cm⁻¹).



1243 Figure S7. Nanoplastics hydrophobicity and surface morphology

- (A) Plot of concentration of Rose Bengal Dye bound to nanoplastics as a function of concentration of the nanoplastics. Error bars represent the mean \pm SD (n=3 independent weathering trials).
- **(B)** Ratio of the amount of hydrophobic dye bound to nanoplastics to the amount of hydrophilic dye bound to nanoplastics.
- (C) Stimulated Emission Depletion (STED) microscope images. Long scale bar = 1 μ m, short scale bar = 200 nm.

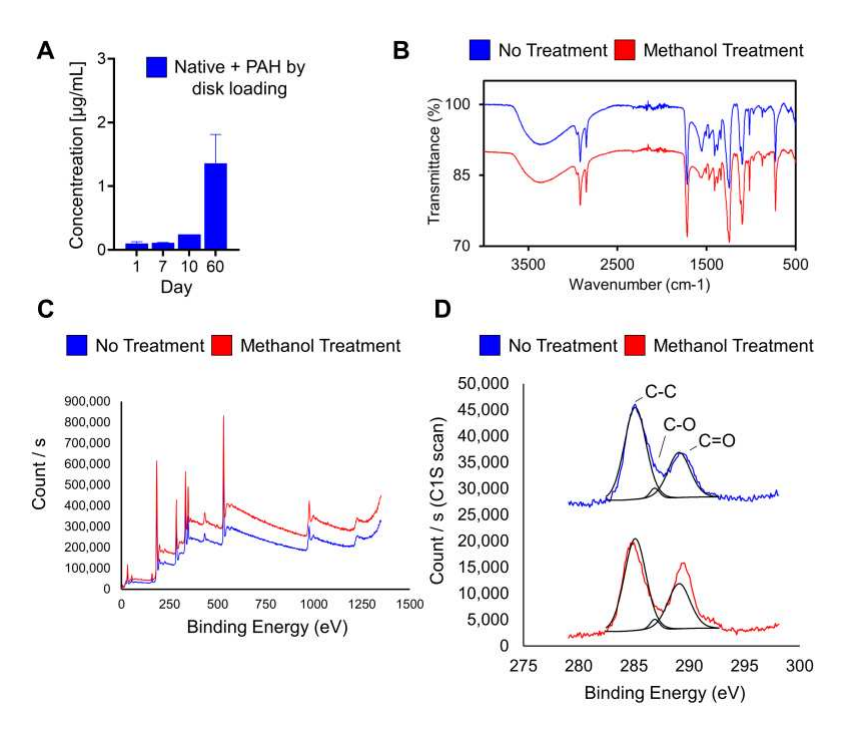


Figure S8. PAH loading protocols, PAH loading for accelerated weathering plastics and ocean plastics

- (A) PAH loading (%) normalized by the total loading observed in Fig. 4a as a function of how long the PAH loading disk was exposed to native nanoplastics in DI water. Error bars represent the mean \pm SD.
- **(B)** FTIR spectra for native nanopastics vs. native nanoplastics soaked in 100% methanol for 3 days. Data has been offset for visualization.
- **(C)** X-ray Photoelectron Spectroscopy (XPS) survey scan recording electron counts per second as a function binding energy (eV) for nanoplastics and nanoplastics treated with methanol.
- **(D)** X-ray Photoelectron Spectroscopy (XPS) C1s scan recording electron counts per second as a function binding energy (eV) for nanoplastics and nanoplastics treated with methanol.

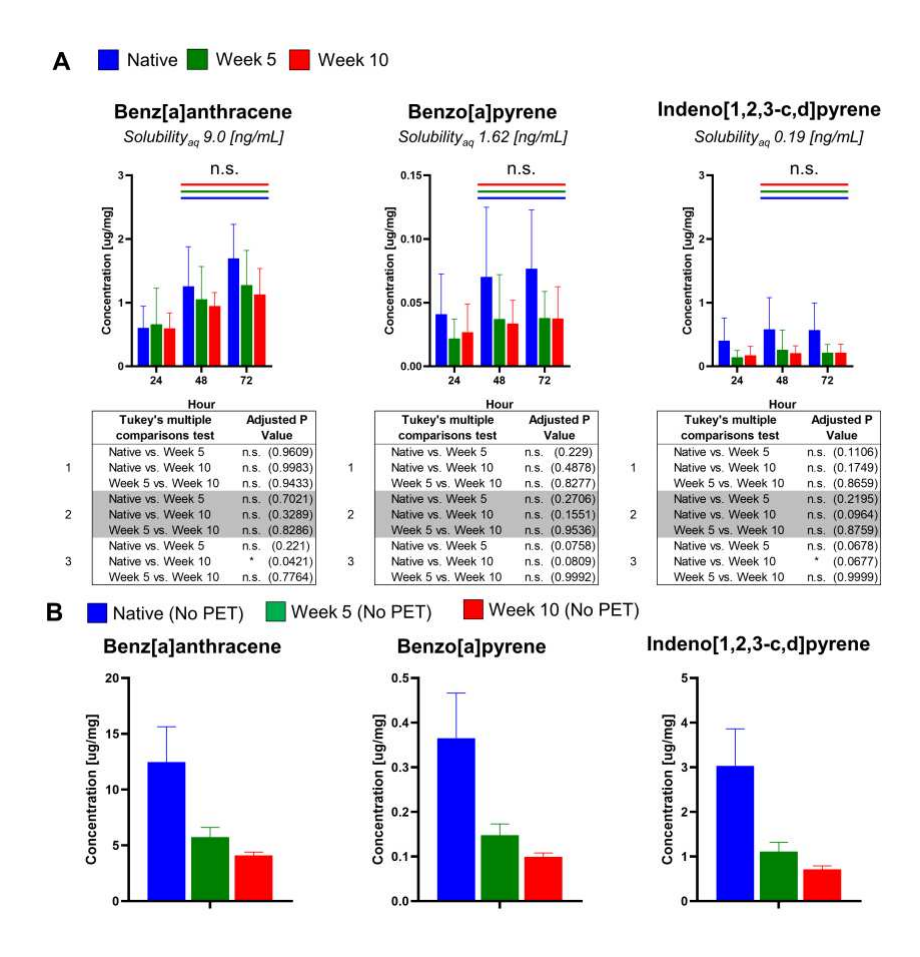


Figure S9. PAH Loading Kinetics

(A) PAH concentration in ug per mg of nanoplastics for native, nanoplastics after photochemical weathering for 5 and 10 weeks days 1, 2, and 3. Published aqueous solubilities of respective PAHs are shown as a function of ng PAH per 1mL of solvent, n = 10. Mann-Whitney tests were performed for the figure to compare day 2 vs. day 3 loading for native, week 5, and week 10, *: p < 0.05, ns: p > 0.05. Tukey's multiple comparison performed for individual time points, *: p < 0.05, ns: p > 0.05. Error bars represent the mean \pm SD.

(B) PAH concentration in ug per mg of nanoplastics devoid of PET for native, nanoplastics after photochemical weathering for 5 and 10 weeks, n = 10.

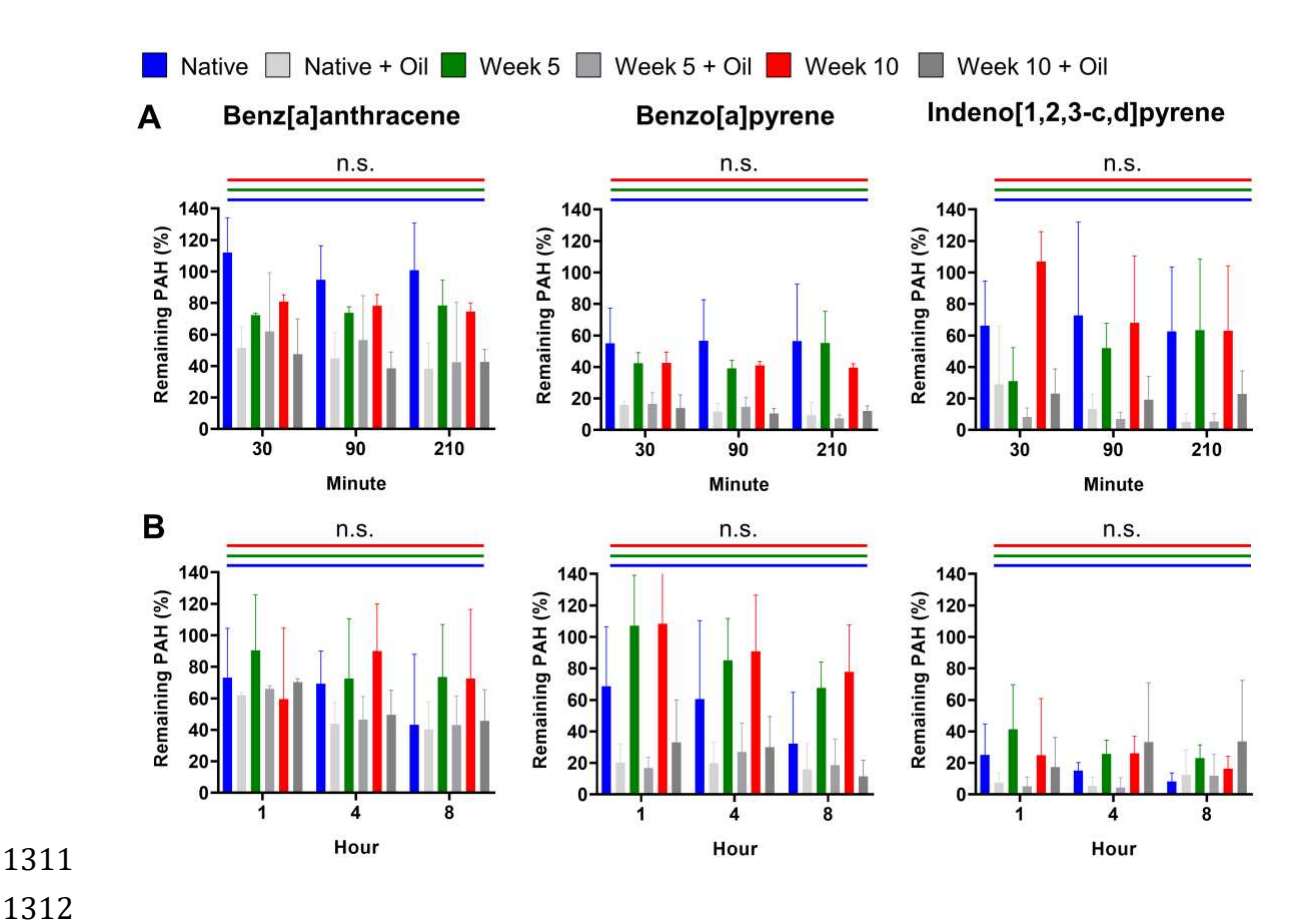


Figure S10. PAH Release and Bioacessibility Kinetics

- (A) Percent of PAHs released from native and nanoplastics after photochemical weathering for 5 and 10 weeks as function of exposure to gastric juices with and without the presence of hydrophobic olive oil. Harvests occurred at 30 min, 90 min, and 210 min. Percentages are with respect to nanoplastics incubated within equivalent volumes of Deionized water, n = 8.
- **(B)** Percent of PAHs released from native and nanoplastics after photochemical weathering for 5 and 10 weeks as function of exposure to intestinal juices with and without the presence of hydrophobic olive oil. Harvests occurred at 1 hour, 4 hours, and 8 hours. Percentages are with respect to nanoplastics incubated within equivalent volumes of Deionized water, n = 8.
- **A-B** 2way ANOVA test was performed for the figure. Comparisons denote the effects of time (row factor). *: p < 0.05, ns: p > 0.05. Error bars represent the mean \pm SD.

Table S1. FTIR Table			
Wavenumber (cm ⁻¹)	Chemical Group		
3560	$\mathrm{OH^4}$		
3440	2 x C=O stretching ⁴		
2970	aliphatic CH2 ⁴		
2916	aliphatic CH ₂ ⁴		
2846	C-H symmetric Stretch		
2513	v1 (in-plane symmetric stretching) & v3 (in-plane asymmetric stretching) 5, 6		
1790	v1 (in-plane symmetric stretching) & v4 (in-plane bending mode) ^{5, 6}		
1721	C=O stretch (ester) ^{4, 7}		
1600-1690 cm-'	aromatic ketones ⁸		
1504-1580	C-C (aromatic), interplane skeletal vibrations of the aromatic ring, vibrations along benzene OCH ₂ CH ₂ O plane ^{4,} 8-10		
1435-1473	CH ₂ bend ^{4, 7}		
1270-1600 (1425)	v ₃ (in-plane asymmetric stretching) ^{5, 6}		
1410	C-C (aromatic) ^{4, 7}		
	ring CH in-plane bending ^{4, 7}		
1367	CH2 wagging 4,7		
1334	Benzene CC, CH π^4		
1286	ring-ester in-plane mode ⁴		
1262	ring induced C(=O)-O stretching mode ^{4, 7}		
1174	ring CH in-plane bending ⁷		
1123	O-CH ₂ stretching crystalline ^{4,7}		
1098	C-O stretching (gauche) ¹⁰		
1018	ring C-H in plane deformation ¹⁰		
971	Benzene along center of symmetry ⁴		
872	v ₂ (out-of-plane bend) ^{5, 6}		
873	C-H (aromatic) out of plane ^{4, 7, 9}		
726	C-H oop wagg AR due to ester ^{4, 7}		
713	ν ₄ (in-plane bending mode) ^{5, 6}		

** Green refers to week 5 FTIR bands and red refers to week 10 specific bands

Table S2. Gastric and Intestinal Juices Composition Table						
Component	Concentration (M)	Composition (%)				
Gastric						
Urea	0.4	0.77%				
Glucuronic acid	0.8	1.54%				
NaH2PO4	1	1.93%				
NH4Cl	1.2	2.32%				
Glucoseamine Hydrochloride	1.4	2.70%				
CaCl2	1.6	3.09%				
HCl	2.6	5.02%				
Glucose	2.6	5.02%				
KCl	3.2	6.18%				
BSA	4	7.72%				
Pepsin	10	19.31%				
NaCl	11	21.24%				
Mucin	12	23.17%				
	Duodenum					
KCl	1.6	0.91%				
NaCl	21	12.00%				
NaHCO3	23.2	13.25%				
Urea	1	0.57%				
CaCl2	1	0.57%				
HCl	0.06	0.03%				
BSA	7.2	4.11%				
Bile	120	68.55%				
	Bile					
KCl	2.26	2.23%				
NaCl	28	27.65%				
NaHCO3	23.2	22.91%				
MgCl2	0.2	0.20%				
KH2PO4	0.32	0.32%				
Urea	0.4	0.40%				
CaCl2	0.8	0.79%				
HCl	0.08	0.08%				
BSA	4	3.95%				
Pancreatin	36	35.55%				
Lipase	6	5.93%				

Table S3. Bioacessibility Stats

Benz[a]anthracene

Sorption

Brown-Forsythe ANOVA test

3.445 (2.000, 25.52) 0.0474 F^* (DFn, DFd) P value
Welch's ANOVA test

W (DFn, DFd) 3.443 (2.000, 17.63) P value 0.0547

Wilcoxon matched-pairs signed rank test

Comparison 0.0273 Native vs W5 W5 vs. W10 0.4922 Native vs. W10 0.0059

Desorption, Gastric

Kruskal-Wallis test rank test Comparison Comparison <0.0001 0.0078 All NP only Native vs Oil W5 vs. Oil 0.0781 0.1 Oil only 0.9324 Native vs. Oil 0.0078

Wilcoxon matched-pairs signed

Desorption, Small Intestine

Wilcoxon matched-pairs signed Kruskal-Wallis test rank test Comparison Comparison All NP only 0.0731 Native vs Oil 0.3828 0.0878 0.6977 0.0781 0.1094 W5 vs. Oil Oil only Native vs. Oil

1338

1339

Benzo[a]pyrene

Sorption

Brown-Forsythe ANOVA test

F* (DFn, DFd) 4.744 (2.000, 17.89)

P value 0.0222

Welch's ANOVA test

W (DFn, DFd) 3.045 (2.000, 16.86) P value 0.0743

Wilcoxon matched-pairs signed rank test

Comparison Native vs W5

0.0137 0.7695 W5 vs. W10 Native vs. W10 0.0039

Desorption, Gastric

Kruskal-V	/allis test	Wilcoxon matched-pairs signed rank test		
Comparison	Р	Comparison		
All	< 0.0001	Native vs Oil	0.0078	
NP only	0.4831	W5 vs. Oil	0.0078	
Oil only	0.827	Native vs. Oil	0.0078	

Desorption, Small Intestine

Kruskal-Wallis test		Wilcoxon matched-pairs signed rank test		
Comparison	Р	Comparison	Р	
All	0.0001	Native vs Oil	0.0234	
NP only	0.1433	W5 vs. Oil	0.0078	
Oil only	0.8781	Native vs. Oil	0.0078	

1340

	Inde	no[1,2,3-c,d]pyrene			
Sorption		Desorption, Gastric			
Brown-Forsythe ANOVA	test	Kruskal-V	Vallis test	Wilcoxon matche	
F* (DFn, DFd)	5.892 (2.000, 12.51)	Comparison	Р	Comparison	
P value	0.0157	All	< 0.0001	Native vs Oil	0.0078
Welch's ANOVA test		NP only	0.2808	W5 vs. Oil	0.0156
W (DFn, DFd)	3.216 (2.000, 16.46)	Oil only	0.075	W10 vs. Oil	0.0156
P value	0.0662				
Wilcoxon matched-pairs	signed rank test				
Comparison					
Native vs W5	0.0137				
W5 vs. W10	0.7695				
Native vs. W10	0.0039				
		Desorption, Small Intestine			
		Kruskal-Wallis test Wilcoxon matched-pairs rank test			
		Comparison	Р	Comparison	Р
		All	0.0355	Native vs Oil	0.6406
		NP only	0.0084	W5 vs. Oil	0.0156

Oil only

0.4712

Native vs. Oil

0.3125

1342

1343

1344

1345

SUPPORTING INFORMATION AND FIGURE REFERENCES

- 1347 1. Doktorovova, S.; Shegokar, R.; Martins-Lopes, P.; Silva, A. M.; Lopes, C. M.;
- Müller, R. H.; Souto, E. B. Modified Rose Bengal Assay for Surface Hydrophobicity
- Evaluation of Cationic Solid Lipid Nanoparticles (Csln). *Eur J Pharm Sci* **2012**, *45* (5), 606-12.
- 1351 2. Müller, R. H.; Rühl, D.; Lück, M.; Paulke, B. R. Influence of Fluorescent
- 1352 Labelling of Polystyrene Particles on Phagocytic Uptake, Surface Hydrophobicity,
- and Plasma Protein Adsorption. *Pharm Res* **1997**, *14* (1), 18-24.
- Rauf, M. A.; Graham, J. P.; Bukallah, S. B.; Al-Saedi, M. A. S. Solvatochromic
- 1355 Behavior on the Absorption and Fluorescence Spectra of Rose Bengal Dye in Various
- Solvents. Spectrochimica Acta Part A: Molecular and Biomolecular Spectroscopy
- 1357 **2009,** *72* (1), 133-137.
- 1358 4. Liang, C. Y.; Krimm, S. Infrared Spectra of High Polymers: Part Ix.
- Polyethylene Terephthalate. *Journal of Molecular Spectroscopy* **1959,** *3* (1), 554-574.
- 1360 5. Xu, B.; Poduska, K. M. Linking Crystal Structure with Temperature-Sensitive
- 1361 Vibrational Modes in Calcium Carbonate Minerals. *Physical Chemistry Chemical*
- 1362 *Physics* **2014**, *16* (33), 17634-17639.
- 1363 6. Andersen, F. A.; Brečević, L. Infrared Spectra of Amorphous and Crystalline
- 1364 Calcium Carbonate. *Acta Chemica Scandinavica* **1991**, *45*, 1018-1024.
- 1365 7. Donelli, I.; Freddi, G.; Nierstrasz, V. A.; Taddei, P. Surface Structure and
- 1366 Properties of Poly-(Ethylene Terephthalate) Hydrolyzed by Alkali and Cutinase.
- 1367 *Polymer Degradation and Stability* **2010,** 95 (9), 1542-1550.
- 1368 8. Edge, M.; Wiles, R.; Allen, N. S.; McDonald, W. A.; Mortlock, S. V.
- 1369 Characterisation of the Species Responsible for Yellowing in Melt Degraded
- 1370 Aromatic Polyesters—I: Yellowing of Poly(Ethylene Terephthalate). *Polymer*
- 1371 *Degradation and Stability* **1996,** *53*, 141-151.

- 1372 9. Alzuhairi, M.; Khalil, B.; Hadi, R. S. Nano Zno Catalyst for Chemical Recycling
- of Polyethylene Terephthalate (Pet). Engineering Technology Journal
- **2017**, *35*, 831-837.
- 1375 10. Sang, T.; Wallis, C. J.; Hill, G.; Britovsek, G. J. P. Polyethylene Terephthalate
- 1376 Degradation under Natural and Accelerated Weathering Conditions. *European*
- 1377 *Polymer Journal* **2020,** *136,* 109873.